WestVirginiaUniversity
THE RESEARCH REPOSITORY @ WVU

Graduate Theses, Dissertations, and Problem Reports

2017

Analysis of Model-Aided Navigation of Unmanned Aerial Vehicles

Stephane D'Urso

Follow this and additional works at: https://researchrepository.wvu.edu/etd

Recommended Citation

D'Urso, Stephane, "Analysis of Model-Aided Navigation of Unmanned Aerial Vehicles" (2017). *Graduate Theses, Dissertations, and Problem Reports*. 5519.
https://researchrepository.wvu.edu/etd/5519

This Thesis is protected by copyright and/or related rights. It has been brought to you by the The Research Repository @ WVU with permission from the rights-holder(s). You are free to use this Thesis in any way that is permitted by the copyright and related rights legislation that applies to your use. For other uses you must obtain permission from the rights-holder(s) directly, unless additional rights are indicated by a Creative Commons license in the record and/ or on the work itself. This Thesis has been accepted for inclusion in WVU Graduate Theses, Dissertations, and Problem Reports collection by an authorized administrator of The Research Repository @ WVU. For more information, please contact researchrepository@mail.wvu.edu.

ANALYSIS OF MODEL-AIDED NAVIGATION OF UNMANNED AERIAL VEHICLES

Stéphane D'Urso

Thesis submitted to the
Benjamin M. Statler College of Engineering and Mineral Resources
at West Virginia University

in partial fulfillment of the requirements for the degree of

Master of Science
in
Aerospace Engineering

Jason Gross, Chair, Ph.D.
Marcello Napolitano, Ph.D.
Patrick Browning, Ph.D.

Department of Mechanical and Aerospace Engineering

Morgantown, West Virginia
2017

Keywords: Aerodynamic Modeling, UAV, Navigation, GPS-Denied

Copyright Stéphane D'Urso © 2017

ABSTRACT

Analysis of Model-Aided Navigation of Unmanned Aerial Vehicles

Stéphane D'Urso

To overcome the rapid and unbounded error growth of low-cost Inertial Navigation Systems (INS), aircraft localization methods commonly compensate for Inertial Measurement Unit (IMU) sensor errors by integrating them with Global Positioning System (GPS) measurements via a Kalman Filter. However, over the past decade, the potential of GPS jamming or even spoofing GPS signals has forced the research community to focus on the development of GPS-denied navigation technologies. Among the GPS-denied techniques, one approach that has been considered is the use of a Vehicle Dynamic Models (VDM) to reduce the rate at which an INS becomes unusable. As such, this Master's thesis considers the use of different aerodynamic modeling approaches to aid in compensation of IMU errors of a fixed-wing Unmanned Aerial Vehicle (UAV). The goals of this research are to evaluate the sensitivity of the performance of dynamic model aided navigation in the context of low-cost platforms where performance benefit must be weighed against the complexity that is required to develop the dynamic model. To do this, first, in simulation, the sensitivity to the required modeling accuracy is shown by perturbing the model coefficients with errors. In addition, different sensors and sensor grades are evaluated, and three different model-aided navigation architectures are discussed and evaluated. To conduct this work, a UAV simulation is developed within which a UAV trajectory is driven by "truth" dynamic model and then IMU measurements are derived and errors are added to them using standard stochastic models for IMU sensors. Finally, the algorithm performance is then evaluated using actual UAV flight testing data from a low cost testbed equipped with GPS and IMU sensors. The testbed used and modeled is a 2.4 m span fixed wing UAV designed and instrumented at WVU.

Acknowledgments

I would like to thank my research advisor, Dr. Jason Gross, for his assistance for the Filtering part of this thesis and for the opportunity to work as a part of his research group.

I would also like to thank my committee members Dr. Marcello Napolitano and Dr. Patrick Browning for reviewing my thesis and providing helpful comments and feedback.

In particular, I would like to acknowledge the contribution of Tanmay Mandal for helping me building the UAV and for his suggestions about the flight testing sessions; at the same time I would like to thank Scott Harper and Nathan Tehrani for helping me prepare the UAV for the flight testing sessions and their help on the field.

I would also like to thank Giuseppe Calise and Rosario Pecora for their advices and valuable support about CFD and VLM respectively.

Finally, I would like to express my deepest thanks to my family and my girlfriend Iole, for their love, their constant support and their fundamental encouragement that have been decisive. Thank you so much!

Contents

Abstract **ii**

Acknowledgments **iii**

List of Figures **vi**

List of Tables **ix**

1 Introduction **1**

1.1 Research motivation 1

1.2 Literature review 1

1.3 Research objective 2

1.4 Thesis outline 2

2 Technical approach **3**

2.1 The testbed UAV 3

2.1.1 Building the aircraft 5

2.1.2 Sensors 6

2.1.3 CAD modeling 7

2.2 Aircraft aerodynamic modeling 9

2.2.1 Coordinate systems 9

2.2.2 Equations of motion 10

2.2.3 VLM 11

2.3 CFD 19

2.3.1 Rough preliminary model validation 22

2.4 Model-Aided Navigation Architecture 24

2.4.1 Vehicle Dynamic Model 24

2.4.2 Inertial Navigation System 25
2.4.3 Filter Design 26

3 Experimental setup **29**
3.1 Flight Simulation 29
3.2 Flight Testing 30

4 Results **33**
4.1 Flight Simulation 33
4.1.1 Model-aided navigation architecture 34
4.1.2 IMU sensor grade 34
4.1.3 UAV dynamic model quality with respect to truth 37
4.2 Flight Testing 40
4.2.1 Model-Aided navigation architecture 40

5 Conclusions **48**

Appendices **49**

A The Testbed parts **1**

B Aerodynamics **4**
B.1 Airfoils 4

List of Figures

2.1 The Phastball Zero aircraft 4
2.2 The Phastball Zero three-views 4
2.3 UAV Initial conditions 6
2.4 Printed parts 6
2.5 Phastball Zero sensors configuration 6
2.6 Reference drawings from 2D (dimensions in millimeters) 7
2.7 Reference section from 3D 8
2.8 Reference section from 2D 8
2.9 CAD model, details and inertia values estimation 8
2.10 CAD model for CFD calculations 9
2.11 VLM reference coordinate system 12
2.12 VLM paneling (isometric view) 13
2.13 VLM paneling top view with paneling labels 13
2.14 VLM paneling side view with paneling labels 13
2.15 VLM mode 1 pressure distribution 14
2.16 VLM mode 2 pressure coefficient distribution 14
2.17 VLM mode 3 pressure coefficient distribution 15
2.18 VLM mode 4 pressure coefficient distribution 15
2.19 VLM mode 5 pressure coefficient distribution 16
2.20 VLM mode 6 pressure coefficient distribution 16
2.21 VLM mode 7 pressure coefficient distribution 17
2.22 VLM pressure distribution for the entire aircraft 17
2.23 VLM pressure distribution for the wing 18
2.24 CFD domain 3D view 19

2.25 CFD domain 2D view with aircraft 19
2.26 CFD mesh 20
2.27 CFD mesh details 20
2.28 Pressure distribution on the whole aircraft at AOA = 0° 20
2.29 Htail airfoil - AOA=0°, $\delta_e = 0°$ 20
2.30 Wall-y+ field at AOA=0° 21
2.31 Streamlines and tip vortices visualization at AOA=10° 21
2.32 Wing airfoil - AOA=0° 21
2.33 Htail airfoil - AOA=0°, $\delta_e = 10°$ 21
2.34 Vortices visualization for AOA=0°, $\delta_e = 10°$ 22
2.35 Vortices visualization for AOA=0°, $\delta_e = 10°$ 22
2.36 Vortices visualization for AOA=10° 23
2.37 Vortices visualization for AOA=10° 23
2.38 3D Datcom model 23
2.39 3D Datcom model views plotted with a DATCOM Pro+ Matlab script 23
2.40 AVL model geometry 24
2.41 AVL model visualizations 24
2.42 Model-Aided Navigation configuration. 26

3.1 FlighGear interface 30
3.2 Louis Bennet Field satellite image (source: Google Maps) 31
3.3 Tail camera image during flight testing 31
3.4 Down looking camera image during flight testing 31
3.5 Ground track 32
3.6 Flight testing trajectories 32

4.1 Position drifts related to the VDM 35
4.2 Velocity drifts related to the VDM 36
4.3 Attitude drifts related to the VDM 36
4.4 Position drifts related to the different aerodynamic models 39
4.5 Attitude drifts related to the different aerodynamic models 39
4.6 Position drifts related of INS alone and MAN (INS+VDM architecture) 41
4.7 Velocity drifts related of INS alone and MAN (INS+VDM architecture) 42
4.8 Attitude drifts related of INS alone and MAN (INS+VDM architecture) 42

4.9 Position drifts related of INS alone and MAN (INS+VDM+Airspeed architecture) . 43
4.10 Velocity drifts related of INS alone and MAN (INS+VDM+Airspeed architecture) . 43
4.11 Attitude drifts related of INS alone and MAN (INS+VDM+Airspeed architecture) . 44
4.12 Position drifts related of INS alone and MAN (INS+VDM+Airspeed+Altimeter architecture architecture) 44
4.13 Velocity drifts related of INS alone and MAN (INS+VDM+Airspeed+Altimeter architecture architecture) 45
4.14 Attitude drifts related of INS alone and MAN (INS+VDM+Airspeed+Altimeter architecture architecture) 45
4.15 Position drifts related of INS alone and MAN (INS+VDM architecture), different Q and R 46
4.16 Velocity drifts related of INS alone and MAN (INS+VDM architecture), different Q and R 46
4.17 Attitude drifts related of INS alone and MAN (INS+VDM architecture), different Q and R 47

B.1 Wing airfoil NACA 2410 4
B.2 Horizontal Tail airfoil NACA 0009 4

List of Tables

2.1 WVU Phastball Zero UAV Characteristics 5

2.2 Measured parameters 7

2.3 Moment of inertia estimated with CATIA V5 8

2.4 VLM coefficients estimated values 18

2.5 Drag coefficients estimated values 23

4.1 Process noise covariance matrix Q and measurement noise covariance matrix R values for Flight Simulation data. 34

4.2 Model-Aided Navigation architectures results 35

4.3 Honeywell HG1930BA50 Performance [23] 37

4.4 IMU sensor grades' results 37

4.5 UAV dynamic model quality results 38

4.6 Process noise covariance matrix Q and measurement noise covariance matrix R values for Flight Testing data. 40

4.7 Model-Aided Navigation architectures results 40

4.8 Model-Aided Navigation architectures results 41

4.9 Process noise covariance matrix Q and measurement noise covariance matrix R values for Flight Testing data INS+VDM only case 47

A.1 HET650-58-1970 (motor) characteristics 1

A.2 ADIS16485 (IMU) characteristics 1

A.3 STI22FS-5 (potentiometer) characteristics 1

A.4 MPXV7002 (pitot) characteristics 1

A.5 OEM 615 (GPS Novatel) characteristics 2

A.6 EVK-M8T (u-blox) characteristics 2

A.7 MOD54415-100IR (NetBurner) characteristics 3
A.8 Spektrum AR12120 (Receiver) characteristics 3
A.9 ISS-D60 (Sun Sensor) characteristics 3
A.10 Spektrum DX9 (Transmitter) characteristics 3

Acronyms

ADM	Aircraft Dynamics Models
AOA	Angle Of Attack
ARW	Angular Random Walk
AVL	Athena Vortex Lattice
CAD	Computer Aided Design
CFD	Computational Fluid Dynamics
CG	Center of Gravity
COESA	Committee on Extension to the Standard Atmosphere
ECEF	Earth Centered Earth Fixed
ECI	Earth Centered Inertial
EKF	Extended Kalman Filter
GNSS	Global Navigation Satellite System
GPS	Global Positioning System
IMU	Inertial Measurement Unit
INS	Inertial Navigation System
MAN	Model-Aided Navigation
MEMS	Micro-Electromechanical System MEMS
NACA	National Advisory Committee for Aeronautics
NED	North East Down
UAV	Unamnned Aerial Vehicle
UM	Unified Model
UKF	Unscented Kalman Filter
VBN	Vision-Based Navigation
VDM	Vehicle Dynamic Model
VLM	Vortex Lattice Method
WVU	West Virginia University

Nomenclature

Symbol	Units	Description
α	deg	Angle of Attack
$\boldsymbol{Æ}$	-	Aspect Ratio
β	deg	Angle of Sideslip
b	m	Wing span
C	-	Aerodynamic coefficient
$\bar{c}$	m	Mean Aerodynamic Chord
c	m	Chord
δ	deg	Control surface deflection
h	m	altitude
I	kg/m^2	Moment of inertia
p	rad/s	Roll rate
q	rad/s	Pitch rate
r	rad/s	Yaw rate
ϕ	rad	Roll angle
θ	rad	Pitch angle
ψ	rad	Yaw angle
ρ	kg/m^3	Air density
$\bar{q}$	Pa	Dynamic Pressure
S	kg/m^2	Wing surface area
T	N	thrust
V	m/s	Velocity
W	kg	Aircraft weight
ω_e	rad/s	Earth Rotation Rate
$\mathbf{x}$	-	State Vector

Subscripts

a	Aileron
r	Rudder
e	Elevator
HT	Horizontal Tail
VT	Vertical Tail
D	Drag
l	Rolling moment
L	Lift
Y	Side force
m	Pitching moment
n	Yawing moment

Chapter 1

Introduction

1.1 Research motivation

The recent development of low-cost electronic devices made the civilian drone applications increasingly widespread and varied other than the existing for both civil and military fields, and many applications, the knowledge of the dynamics of these drones can play a key role (e.g. in video surveillance). The motivation of this work is to provide further evidence of the benefits of using flight dynamic models in order to estimate position, velocity and attitude estimating using low-cost sensors and simplified aerodynamic models. This approach could be used to enhance GPS/INS systems, to mitigate period of poor GPS reception, or could be combined with completely GPS-denied technologies, such as camera or LIDAR based Simultaneous Localization and Mapping (SLAM).

1.2 Literature review

Multiple authors have previously considered model-aided navigation. Koifman, M. and Bar-Itzhack introduced an approach in which the model of aircraft dynamics, mathematically modeled and coupled with Extended Kalman Filter (EKF), is added to a conventional Inertial Navigation System (INS) to obtain a navigation system with performances considerably better than simply allowing the INS to drift[1]. In this study, it is demonstrated that the dynamics aided INS is more accurate than the unaided INS and, at the same time, that this aided navigation technique allows better calibration of its own error sources if combined with a GPS system. Crocoll et al. [2] introduced an Unified Model (UM) that implicitly constrains the two independent state prediction models (i.e. Vehicle Dynamics Models VDM and INS) to reduce computation burden and state vector when implementing model-aided navigation. Crocoll et. al [3] then used the same UM technique for an

experimental quadcopter application in which they demonstrated that even though no rotational vehicle dynamics are modeled (they use only translational dynamics modeling), roll angles, pitch angles and even IMU biases with bounded errors are estimable with model-aided navigation. Further, for fixed wing aircraft, Bryson and Sukkarieh[4], considered using a VDM to predict the aircraft state vector which are then fused with the IMU measurements via an Extended Kalman filter to estimate the errors in the inertial sensors and in the VDM computations. In this work, they showed that the simulation results related to the different INS configurations considered improves the navigation system performance even when small parameter errors are present in the model. Further, it is shown that IMU bias estimation depends mainly on sudden acceleration errors in the VDM and also on growing errors in the VDM velocity and Euler angles. More recently Cappello et. al [5] combines VDM, called Aircraft Dynamics Models (ADM), with Global Navigation Satellite System (GNSS), Micro-Electromechanical System based Inertial Measurement Unit (MEMS-IMU) and Vision-Based Navigation (VBN) sensors and relative different combinations of them in order estimate position, velocity and attitude for the Aerosonde RPAS UAV also in the context of precision approach and landing phases. Khaghani and Skaloud [6] use a conventional INS/GNSS setup where position, velocity, and attitude are estimated using a VDM and an EKF considering at the same time wind and GNSS outages too.

1.3 Research objective

Considering the previous works and promising results cited above, this thesis will provide additional insight as to the required quality of the UAV dynamic model, and in turn the required fidelity of the modeling approach, as well as determining how much the sensors grade and the model-aided navigation architecture performance affects the velocity, position and attitude estimations.

1.4 Thesis outline

This thesis is organized as follows. Chapter 1 is related to the thesis motivation and objective, and the literature review. Chapter 2 of this thesis is relative to the testbed description, CAD modeling and the different Aerodynamic approach used used to build the reference VDM. The last part of this chapter describes the architectures considered giving a brief decription of classical INS formulations, insights of the VDM and the filter developed. Chapter 3 discusses the two different experimental setups used, the 6DoF flight simulator created and the flight testing. Finally, Chapter 4 and Chapter 5 provide the results obtained considering all the case studies investigated and the conclusions.

Chapter 2

Technical approach

Parts of this chapter are taken from the conference paper "Sensitivity of Unmanned Aerial Vehicle Model-Aided Navigation"[7]

The following section describes the steps performed in order to compute the designed Model-Aided Navigation (MAN) architectures. The first step has been to build and instrument the testbed for flight testing and, at the same time, to create detailed Computer Aided Design (CAD) models. Once all the geometrical, mass, and inertia properties were estimated, different numerical methods were used to create the aerodynamic model of the aircraft. The reference model is based on the Vortex Lattice Method (VLM) and Computational Fluid Dynamics (CFD). The VLM provides all the aerodynamic coefficients and stability derivatives except the drag ones and the velocity body u-component coefficients which are been estimated though the CFD. Preliminary results from other techniques and codes, like System Identification, DATCOM and Athena Vortex Lattice (AVL) have been considered to check the reference model values. This reference model provides the coefficients and parameters that have to be used in the VDM. Then the VDM and the INS are considered as the two subsystems of the proposed MAN architectures.

2.1 The testbed UAV

The aircraft used is a testbed called Phastball Zero, the first modified version of a the Phastball aircraft designed for a Design, Build and Fly competition back in 2009. This plane was constitued, at the beginning of this master thesis, only by the fuselage, wing and tail. Therefore, the first step of this work has been to perform the platform integration and assembly and lately the maintenance.

The Phastball is a fixed-wing aircraft with T-tail empennage configuration, electrically powered and tricycle gear (with wheel pants at the main landing gear to protect the engines from the runaway debris) as shown in Figure (2.1).

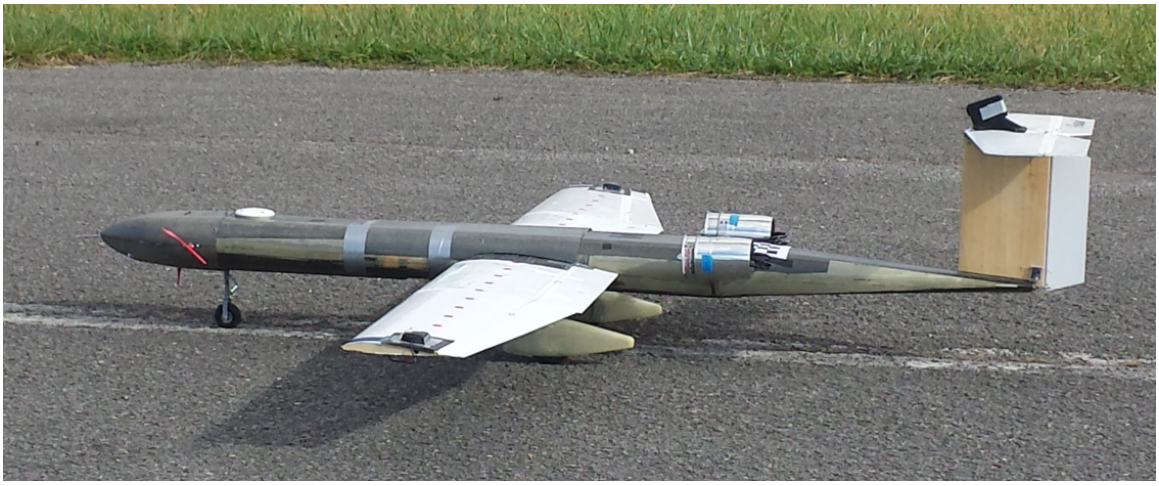

Figure 2.1: The Phastball Zero aircraft

The aircraft has NACA airfoils (as shown in Figure (B.1) and Figure (B.2)) in Appendix B.1) for the wing and horizontal tail respectively a NACA 2410 and NACA 0009 while it has a flat rounded (at the leading and trailing edges) plate of 12 mm thickness as the vertical tail airfoil.

The full-equipped aircraft has an average weight of approximately 12 kg with the center of gravity position at approximately 25% of the mean aerodynamic chord.

The geometric characteristics of the Phastabll Zero as shown in Figure (2.2) and Table 2.1.

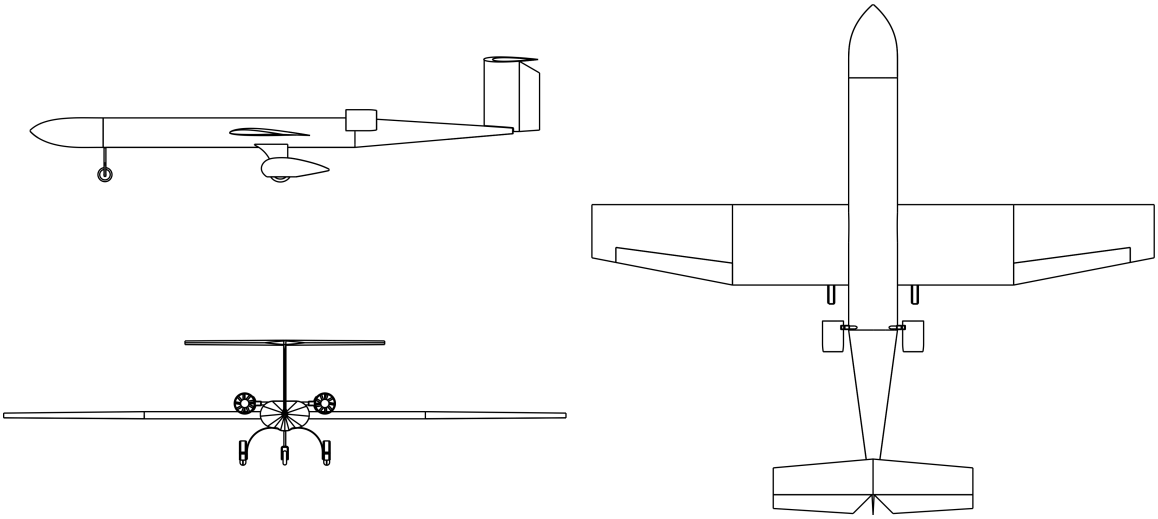

Figure 2.2: The Phastball Zero three-views

The fuselage is with made of carbon fiber, the horizontal tail and the wing are made of fiberglass and extruded polystyrene foam insulation (the wing has, in addition, a carbon fiber reinforcement in the center part) and the vertical tail is made of wood. The aircraft is equipped with 2 electric ducted motors HET650-58-1970, which characteristics are shown in Table A.1.

Table 2.1: WVU Phastball Zero UAV Characteristics

General Characteristics		
Length	l	1.97 m
Height	h	0.55 m
Weight	W	12 kg
Wing Mean Aerodynamic Chord	$\bar{c}$	0.31 m
CG position (x-axis)	x_{CG}	0.25 $\bar{c}$
Lifting Surfaces		
Wing surface	S	0.75 m^2
Wing span	b	2.40 m
Wing Aspect Ratio	$Æ$	7.70
Wing root chord	$c_{r,\mathrm{W}}$	0.35
Wing tip chord	$c_{t,\mathrm{W}}$	0.23
Horizontal Tail surface	S_{HT}	0.18 m^2
Horizontal Tail span	b_{HT}	0.76 m
Horizontal Tail root chord	$c_{r,\mathrm{HT}}$	0.19
Horizontal Tail tip chord	$c_{t,\mathrm{HT}}$	0.21
Vertical Tail surface	S_{VT}	0.01 m^2
Vertical Tail span	b_{VT}	0.30 m
Performance		
Cruise speed	V	25 m sec
Maximum thrust	T	60 N
Airfoils		
Wing Airfoil		NACA 2410
Horizontal Tail		NACA 0009
Vertical Tail		flate plate (12 mm)

2.1.1 Building the aircraft

As stated in the previous section, at the beginning of this research project, Phastball Zero had only its main components (fuselage, wing and tail) as shown in Figure (2.3), so the first step has been to supply the missing parts (like wheel, landing gears, wheel pants, etc.), and take care of the assembly and the platform integration. Some custom parts has been designed and 3D printed as shown in Figure (2.4).

Figure 2.3: UAV Initial conditions

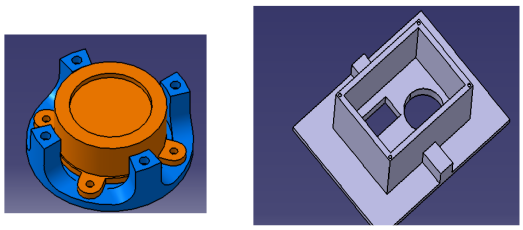

Figure 2.4: Printed parts

2.1.2 Sensors

The configuration realized allows to collect in flight, at the same time, data relative to pilot commands, angle of attack, sideslip angles, atmosphere, GPS, sun sensor (that get the sun incidence angle to be used to estimate the aircraft orientation) and video. The data acquisition system collects data through a NetBurner device at 50 Hz while the GPS module at 10 Hz[8]. This experimental setup has been tested for other WVU researches too[9].

The sensors setup created is shown in Figure (2.5). Details of the sensors are listed in Appendix A. The list of the measured parameteres is shown in Table (2.2).

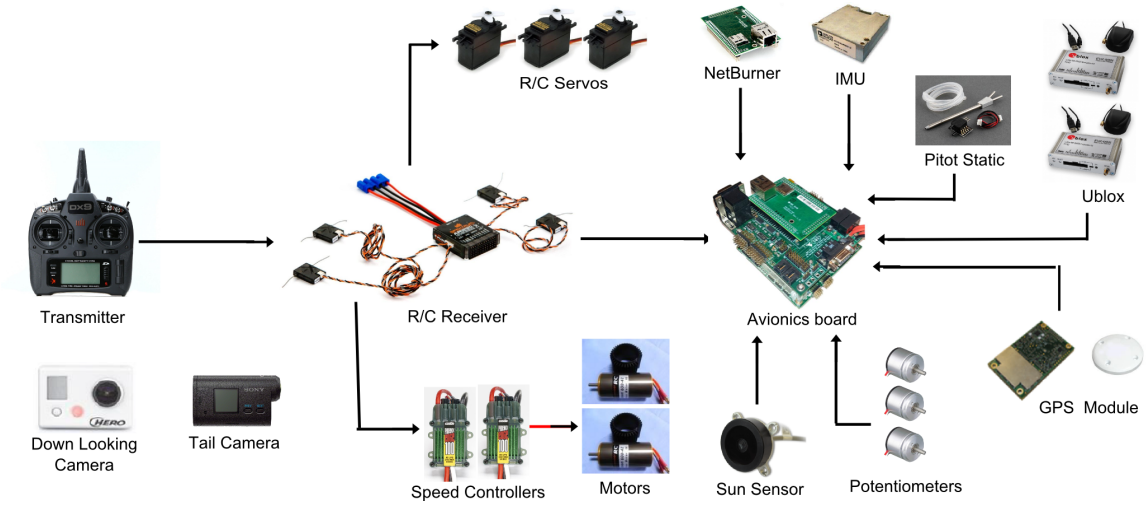

Figure 2.5: Phastball Zero sensors configuration

Table 2.2: Measured parameters

	Pitot	Potentiometers	IMU	GPS modules	Netburner
Airspeed	✓	-	-	-	-
Angle of attack	-	✓	-	-	-
Sideslip angle	-	✓	-	-	-
Pilot commands	-	-	-	-	✓
Accelerations	-	-	✓	-	-
Angular rates	-	-	✓	-	-
Position	-	-	-	✓	-

2.1.3 CAD modeling

The CAD modeling work has been fundamental in order to obtain different information about the plane and to prepare the pre-processing of the various tools and approaches used.

A 2D model, Figure (2.6), has been created to obtain the input values for VLM paneling and DATCOM input.

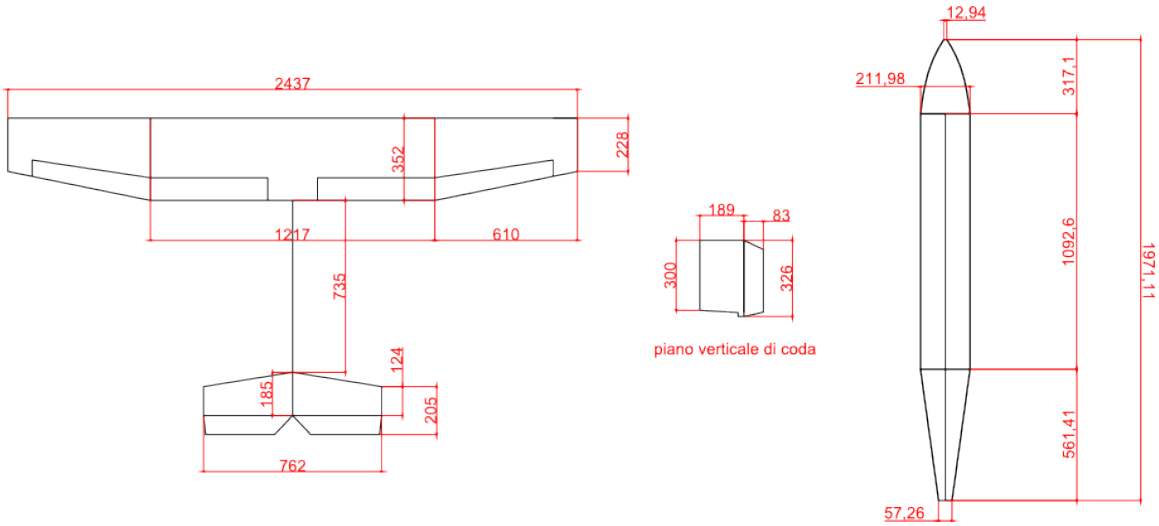

Figure 2.6: Reference drawings from 2D (dimensions in millimeters)

The fuselage section values need to draw the fuselage in Datcom are generated from a 3D as shown in Figure (2.7) and Figure (2.8).

A 3D model, as much detailed as possible, Figure (2.9), has been created to estimate the mass moments of inertia in Table 2.3. The densities for all the components has been considered as uniformly distributed. Wiring has not been taken into account directly drawing them but considering an extra mass for the wing and fulselage (because these wires are present along the entire fuselage lenght and wing span).

The simplified 3D model in Figure (2.10) has been used to perform the CFD calculations. This

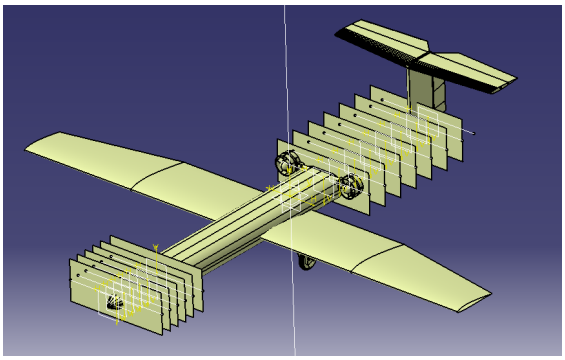

Figure 2.7: Reference section from 3D

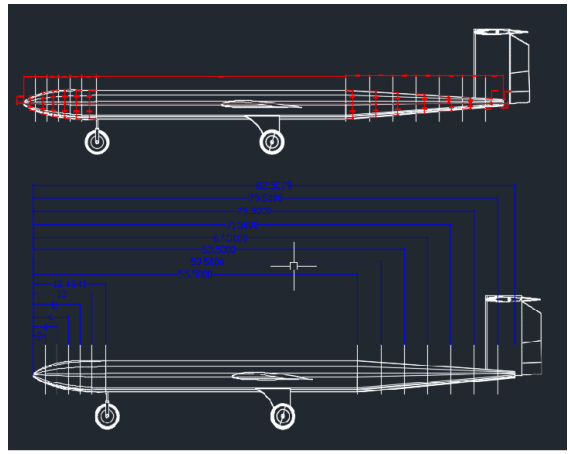

Figure 2.8: Reference section from 2D

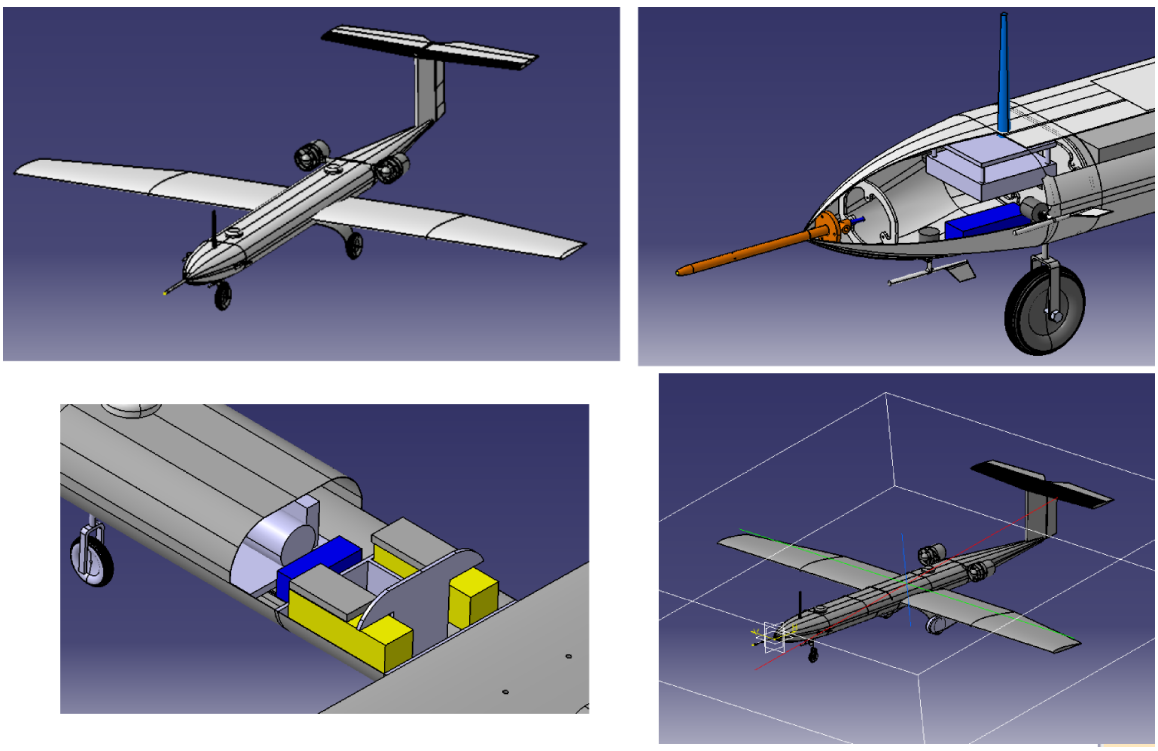

Figure 2.9: CAD model, details and inertia values estimation

Table 2.3: Moment of inertia estimated with CATIA V5

Moment of inertia about x body axis	I_{xx}	$0.96\,\mathrm{kg/m^2}$
Moment of inertia about y body axis	I_{yy}	$2.91\,\mathrm{kg/m^2}$
Moment of inertia about z body axis	I_{zz}	$3.64\,\mathrm{kg/m^2}$
Product of inertia in x-z body axis plane	I_{xz}	$0.20\,\mathrm{kg/m^2}$

model doesn't take into account all the GPS antenna, vanes and the Pitot probe; at the same time all the gaps (e.i. between the wheels and the wheel pants) have been filled. This simplifications were

required in order to properly mesh the CFD model.

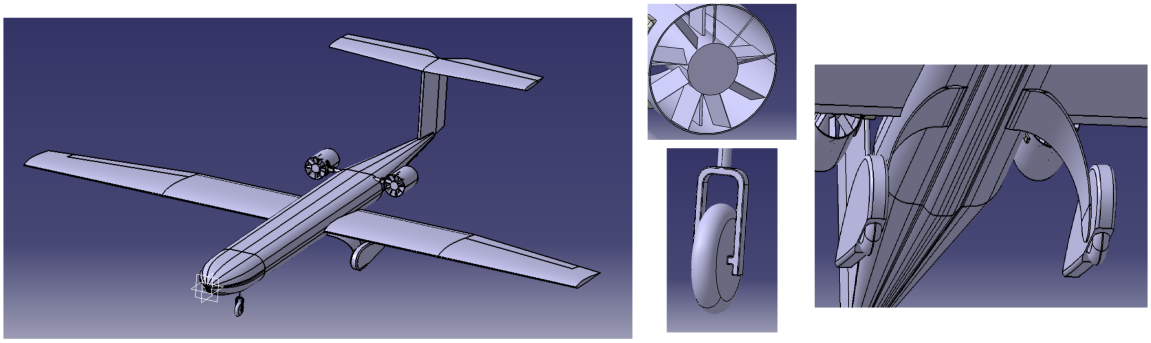

Figure 2.10: CAD model for CFD calculations

2.2 Aircraft aerodynamic modeling

The application of the VDM allows to estimate velocity and attitude through the equations of motion. These equations require the knowledge of the aerodynamic coefficients and the stability derivatives of the aircraft.

The first step for the development of each model was to define the operating points and the reference Reynolds numbers as shown in Appendix B knowing the Phastball Zero UAV speed and airfoil geometry.

2.2.1 Coordinate systems

Four different coordinates sytsems are mentioned in the present work: Earth-Centered Earth-Fixed (ECEF), North East Down (NED), Body axes and Wind axes.

The ECEF has the center corresponding with the Earth center, the z-axis towards the North, the x-axis on the equatorial plane towards the point with longitude and latitude equal to zero and the y-axis towards the needed direction to build this system as a right handed one.

The NED system has its center corresponding with the aircraft center of gravity (CG), and the North, East and Down directions corresponding to the Earth North and East directions and the Down directions towards the vector pointing toward the center of the Earth.

The Body axis is a integral with the aircraft motion, with its center corresponding to the aircraft CG. The x-axis is contained in the aircraft longitudinal plane and it is considered positive pointing forward (nose direction). The z-axis, pointing the same direction as the head-feet pilot direction, is contained in the same longitudinal plane and it is perpendicular to the x-axis. The y-axis, positive

towards the right aircraft wing, is made in order to have a left handed system.

The Wind axis is a left-handed coordinate system, with the aircraft CG corresponding to its center, the x-axis corresponding to the wind direction (positive towards the direction of the motion of the plane). The z-axis, pointing downwards, is contained in the intersection of the vertical plane composed by the wind vector and CG with the perpendicular plane containing the aircraft trajectory. The y-axis is made in order to have a left handed system.

2.2.2 Equations of motion

The reference rigid-body equations of motion are[10] referred to the Body axis:

$$\dot{u} = rv - qw + gx + (F_x/m) \tag{2.1}$$

$$\dot{v} = pw - ru + gy + (F_y/m) \tag{2.2}$$

$$\dot{w} = qu - pv + gz + (F_z/m) \tag{2.3}$$

$$\dot{p} = \frac{\{I_{zz}\ l + I_{xz}\ N - [I_{xz}\ (I_{yy} - I_{xx} - I_{zz})]\ pq + [I_{xz}^2 + I_{zz}\ (I_{zz} - I_{yy})]rq\}}{(I_{xx}\ I_{zz} - I_{xz}^2)} \tag{2.4}$$

$$\dot{q} = \frac{1}{I_{yy}}\ [M - (I_{xx} - I_{zz})\ pr - I_{xz}\ (p^2 - r^2)] \tag{2.5}$$

$$\dot{r} = \frac{\{I_{xz}\ l + I_{xx}\ N - [I_{xz}\ (I_{yy} - I_{xx} - I_{zz})]\ rq + [I_{xz}^2 + I_{xx}\ (I_{xx} - I_{yy})]rq\}}{(I_{xx}\ I_{zz} - I_{xz}^2)} \tag{2.6}$$

$$\dot{\phi} = p + (q \sin\phi + r \cos\phi) \tan\theta \tag{2.7}$$

$$\dot{\theta} = q \cos\phi - r \sin\phi \tag{2.8}$$

$$\dot{\psi} = (q \sin\phi + r \cos\phi) \sec\theta \tag{2.9}$$

where the rate of change of translational velocity is defined from equations 2.1 to 2.3, the rate of change of angular velocity is defined from equations 2.4 to 2.6 and the rate of change of Angular position is is defined from equations 2.7 to 2.9. In these equations, m is the aircraft mass, p,q and r represent the body-axis angular rates, u, v and w are the body-axis velocity components, ϕ, θ and ψ are the Euler roll, pitch and yaw angles. Also the vector $[F_x\ F_y\ F_z]^T$ represent the aerodynamic and thrust force while the vector $[L\ M\ N]^T$ is the aerodynamic and thrust moment.

The gravitational acceleration g_n is defined in equation (2.10).

$$g_n = \begin{bmatrix} g_x \\ g_y \\ g_z \end{bmatrix} = \begin{bmatrix} -g\sin\theta \\ g\sin\phi\cos\theta \\ g\cos\phi\cos\theta \end{bmatrix} \tag{2.10}$$

The total aerodynamic and thrust force terms and the aerodynamic thrust and moment terms are expressed by:

$$F_x = C_X\bar{q}S + T_x \tag{2.11}$$

$$F_y = C_Y\bar{q}S + T_y \tag{2.12}$$

$$F_z = C_Z\bar{q}S + T_z \tag{2.13}$$

$$l = C_l\bar{q}Sb + M_{T_x} \tag{2.14}$$

$$M = C_M\bar{q}Sc + M_{T_y} \tag{2.15}$$

$$N = C_N\bar{q}Sb + M_{T_z} \tag{2.16}$$

where $\bar{q} = (1/2)\rho V^2$ is the dynamic pressure, ρ is the atmospheric density, S is the wing surface and T, M_T are the thrusting effects.

2.2.3 VLM

The Vortex Lattice Method (VLM) represents the lifting surfaces and their trailing wakes as single -layer vortex sheets, discretized into horseshoe vortex filaments, whose trailing legs are assumed to be parallel to the UAV body x-axis. VLM results are known to be high fidelity, offering detailed information, such as surface loading[11].

It has been used an in-house, non-commercial software which has been developed and upgraded at University of Naples "Federico II" and the Centro Italiano Ricerche Aerospaziali (CIRA) used for static and and dynamic aeroelastic and aero-servo-elastic analysis of aircraft. This software is based on multidisciplinary computational environment based on numerical methods and rational approaches compliant with EASA standards CS-25 and CS-23.

The reference coordinate system for the vector quantities is shown in figure (2.11).

Knowing the aircraft geometry and the flight conditions, each lifting surface was paneled, as shown in Figure (2.12),(2.13) and (2.14)- The aerodynamic mesh is characterized by 35 flat panels (boundaries represented by means of thick lines) and 412 boxes; 19 panels/364 boxes have been used

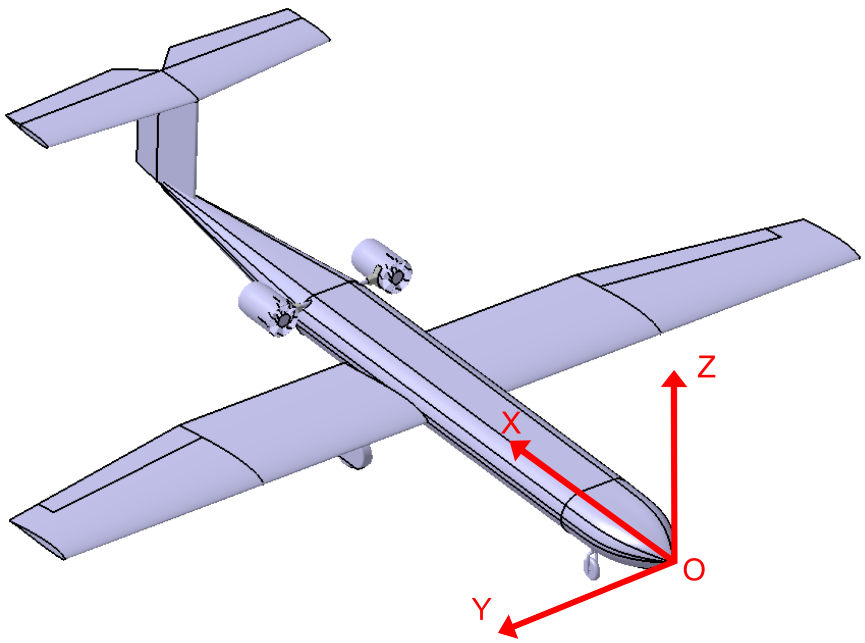

Figure 2.11: VLM reference coordinate system

to model all lifting surfaces (including fuselage contribute) while 8 panels/48 boxes have been used to model the engines nacelles. The fuselage and the engines have been considered in the VLM model in order to account for their interference on lifting surfaces pressures.

The load condition considered refers to the CG position at 25% of the mean aerodynamic chord, aircraft speed of 30 m/s, sea level and unitary load factor.

To calculate the needed coefficients, several "modes" have been analyzed. More precisely, in order to get the aerodynamic pressure at each box, the 3D inviscid flow equations were solved in correspondence of:

- angle of attack equal to zero
- unitary angle of attack (1 radian rotation)
- unitary elevator rotation
- unitary aileron rotation
- unitary rudder rotation
- unitary roll rotation
- unitary yaw rotation

Effects of the wing washout and the airfoils curvature is also considered.

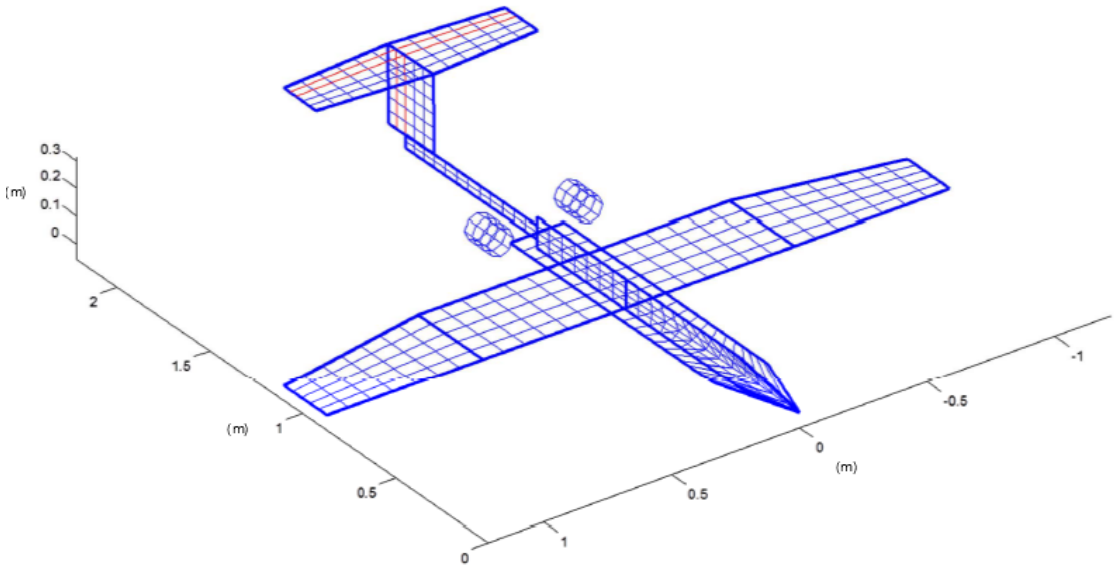

Figure 2.12: VLM paneling (isometric view)

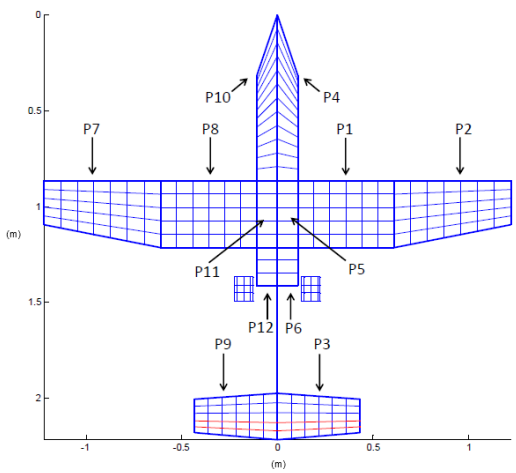

Figure 2.13: VLM paneling top view with paneling labels

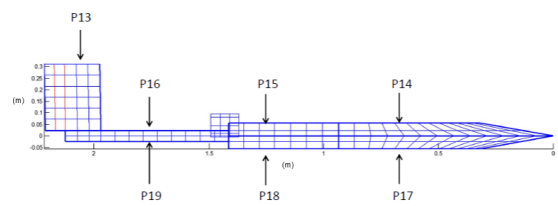

Figure 2.14: VLM paneling side view with paneling labels

The first mode is relative to unitary incidence; its pressure distribution is shown in Figure (2.15). The second one is relative to unitary rotation of the elevator; its pressure distribution is shown in Figure (2.16). The third one is relative to the washout of the wing and the airfoils; its pressure distribution is shown in Figure (2.17). The fourth one is relative to the unitary rotation of the ailerons; its pressure distribution is shown in Figure (2.18) . The fifth one is relative to the unitary rotation of the rudder; its pressure distribution is shown in Figure (2.19). The sixth one is relative to the unitary roll rotation; its pressure distribution is shown in Figure (2.20). The seventh one is relative to the unitary yaw rotation; its pressure distribution is shown in Figure (2.21).

Then these unitary pressure distributions were integrated along the wing and horizontal tail

span with the aim to get the forces and moments distributions as well as the aircraft aerodynamic derivatives and unitary normal forces distributions along the wing and horizontal tail span.

Then the VLM estimates the pressure distribution as shown in Figure (2.22) and Figure (2.23).

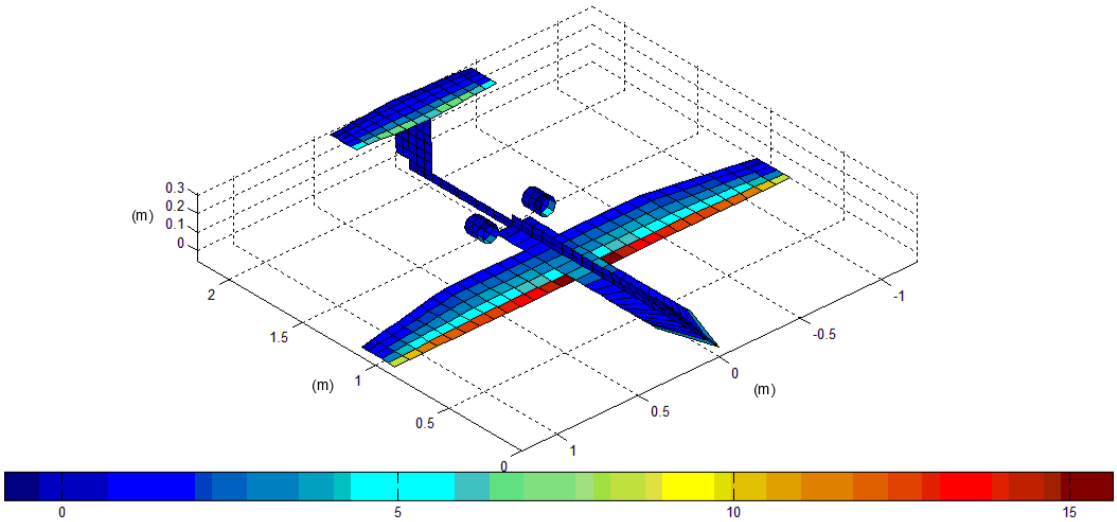

Figure 2.15: VLM mode 1 pressure distribution

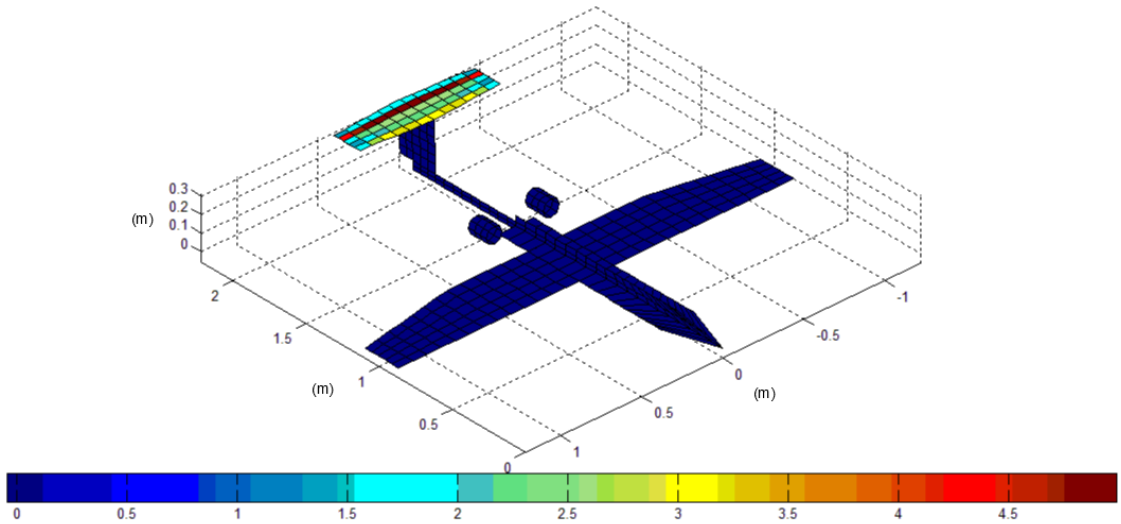

Figure 2.16: VLM mode 2 pressure coefficient distribution

The estimated coefficients are listed in the following Table 2.4.

These results made possible to check that, for this aircraft, all the stability criteria are satisfied[12]. In fact C_{Y_β}, C_{M_α}, C_{l_p}, C_{M_q}, $C_{N_{\delta_r}}$ and C_{l_β} are negative while C_{L_α}, C_{N_β} and C_{M_u} are positive.

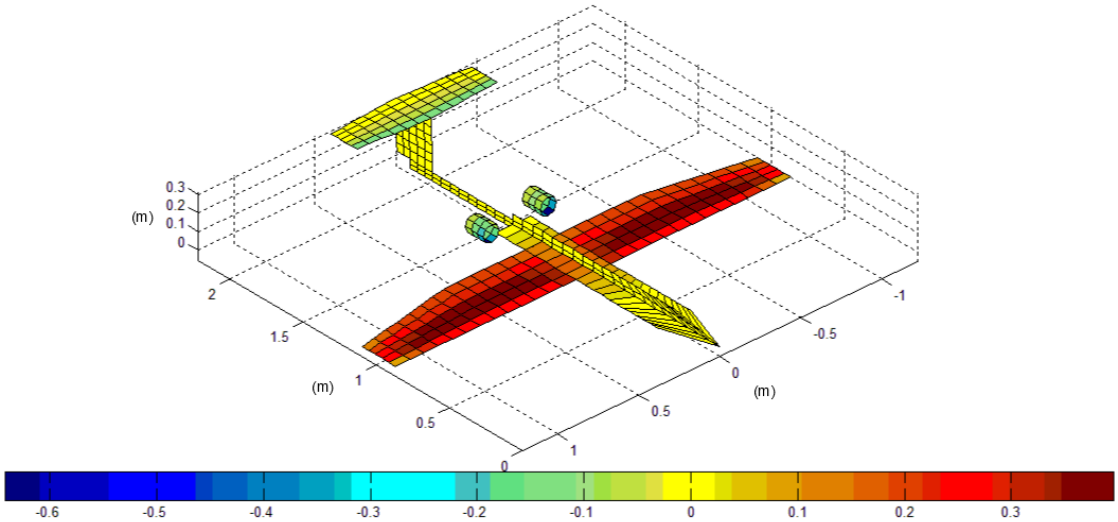

Figure 2.17: VLM mode 3 pressure coefficient distribution

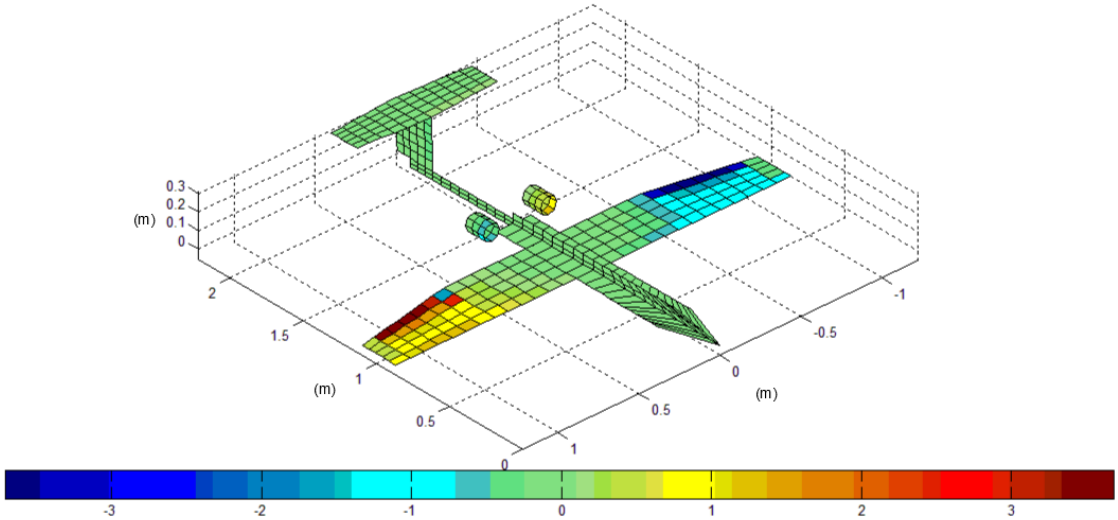

Figure 2.18: VLM mode 4 pressure coefficient distribution

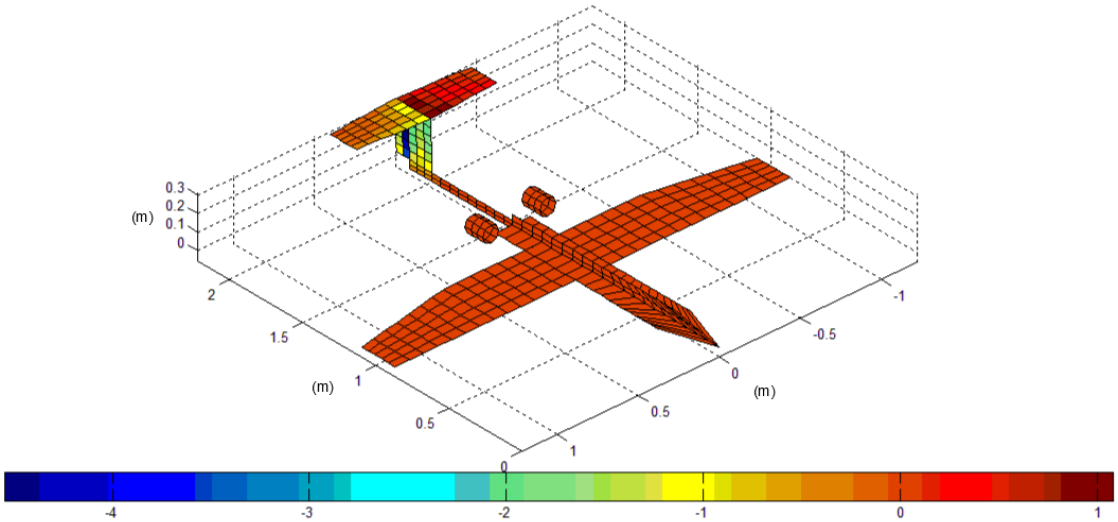

Figure 2.19: VLM mode 5 pressure coefficient distribution

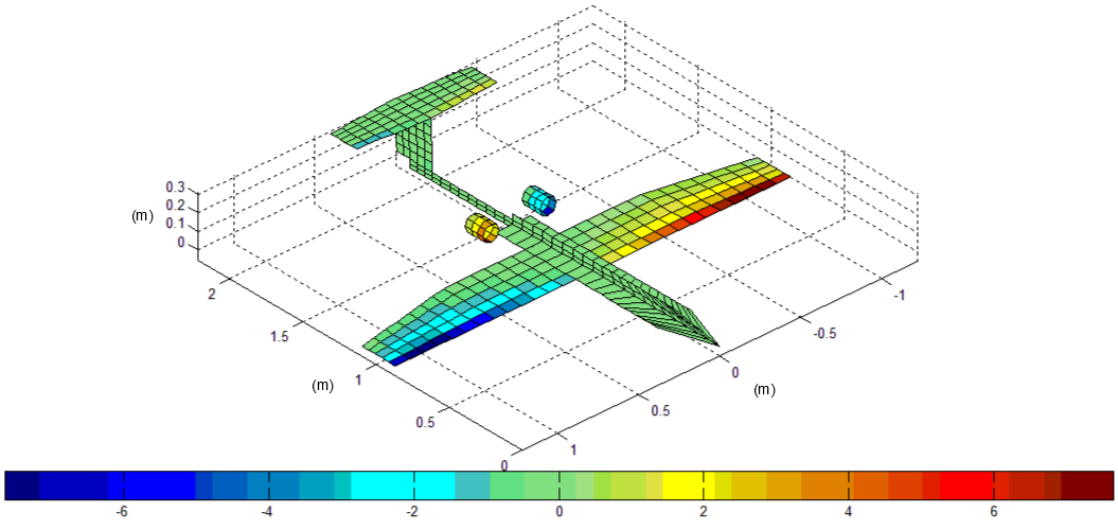

Figure 2.20: VLM mode 6 pressure coefficient distribution

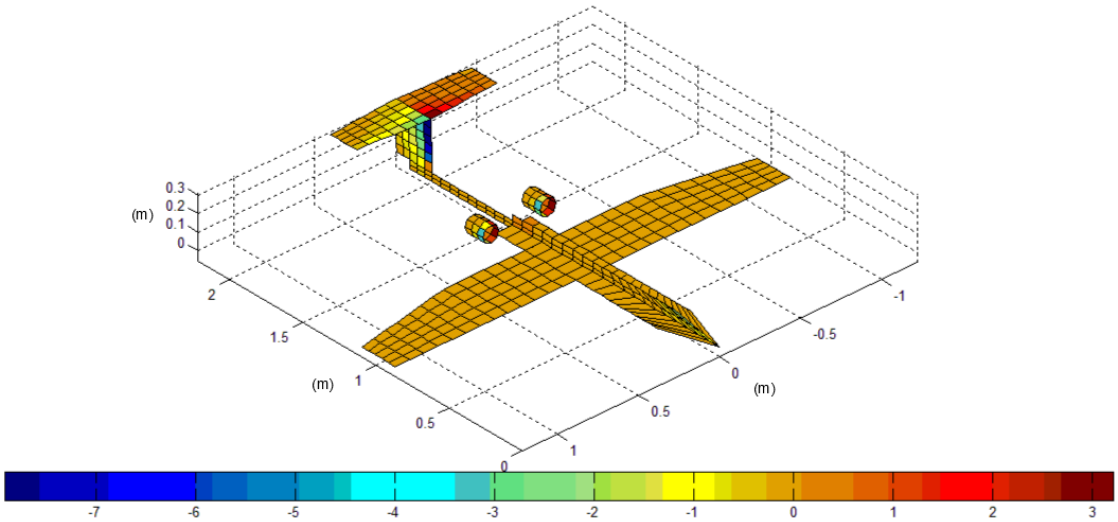

Figure 2.21: VLM mode 7 pressure coefficient distribution

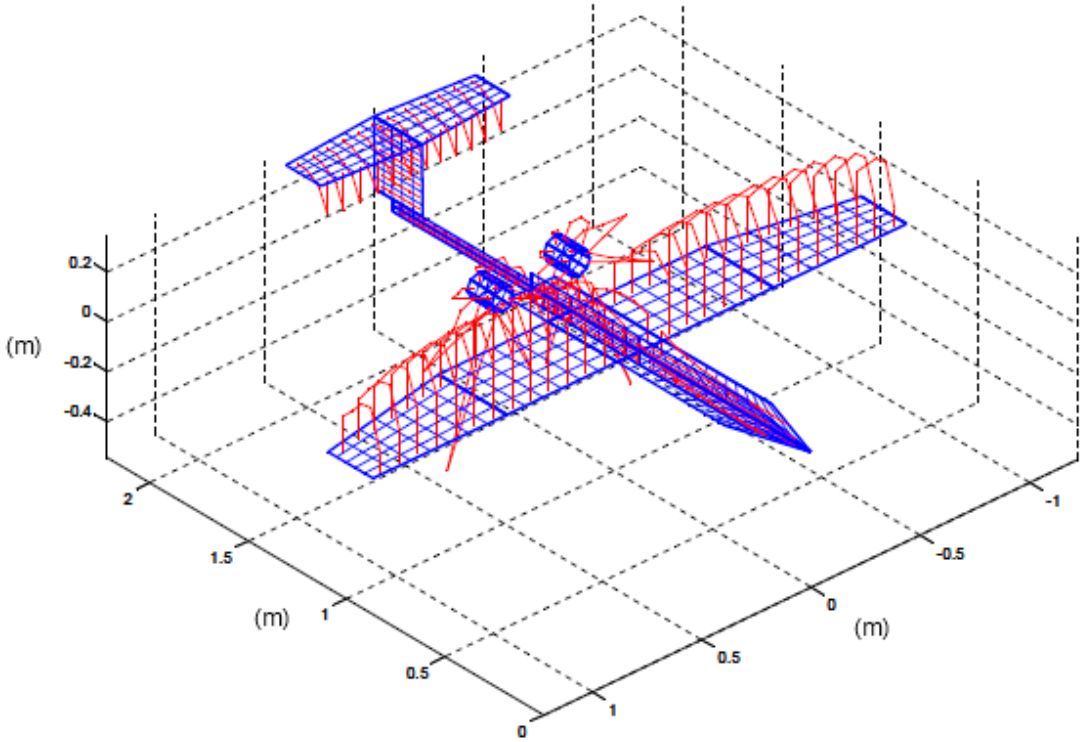

Figure 2.22: VLM pressure distribution for the entire aircraft

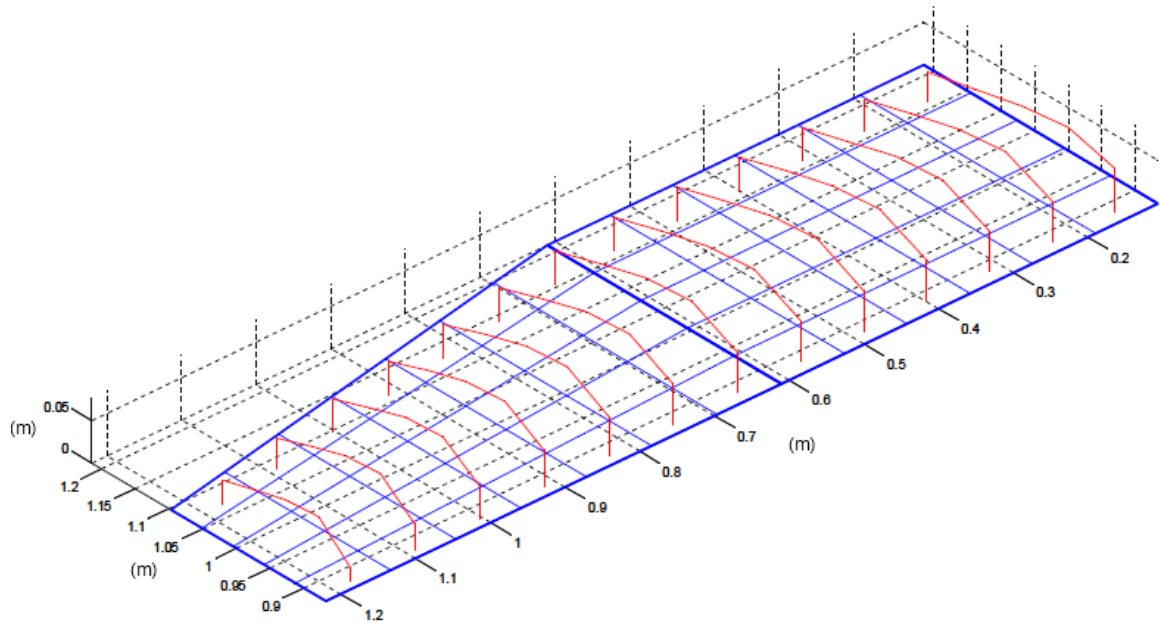

Figure 2.23: VLM pressure distribution for the wing

Table 2.4: VLM coefficients estimated values

VLM aerodynamic coefficients			
C_{L_0}	0.2176	C_{N_r}	-0.1539
C_{L_α}	5.4966	C_{N_p}	-0.0090
$C_{L_{\dot{\alpha}}}$	1.3998	C_{N_β}	0.1098
C_{L_q}	11.2917	$C_{L_{\delta_e}}$	0.6013
C_{M_0}	-0.0029	$C_{M_{\delta_e}}$	-2.0044
C_{M_α}	-1.4361	$C_{Y_{\delta_a}}$	0.0282
$C_{M_{\dot{\alpha}}}$	-6.6338	$C_{Y_{\delta_r}}$	0.2150
C_{M_q}	-20.5535	$C_{l_{\delta_a}}$	0.3068
C_{Y_β}	0.4723	$C_{l_{\delta_r}}$	-0.0210
C_{Y_p}	-0.0266	$C_{N_{\delta_a}}$	0.0113
C_{Y_r}	-0.3710	$C_{N_{\delta_r}}$	0.1003
C_{l_β}	-0.0382	$C_{Y_{\delta_r}}$	0.2150
C_{l_p}	-0.5113	$C_{l_{\delta_r}}$	-0.0210
C_{l_r}	0.0343	$C_{N_{\delta_r}}$	0.1003

2.3 CFD

In order to evaluate the drag coefficient, a CFD computation has been performed using STAR CCM+. The domain has been created considering a spheric environment with a radius of 30 times the length of the aircraft chord as shown in Figure (2.24) and (2.25). This assumption satisfy the software recommended domain setting (the "domain extents around 8–10 body lengths or wing spans"). The use of a spherical far field allows to simulate different angle of attack (AOA) using the same mesh: in other words, different AOAs are simulated changing the direction of the inlet velocity vector. Otherwise, each physical rotation of the aircraft requires the mesh to be generated again. The fluid computational domain has been obtained subtracting the aircraft to the spherical computational domain. Hence, the computational domain is bounded by the far field and aircraft surfaces. Moreover, all the surfaces related to the aircraft have been split (e.g., wing, tail plane, ...) in order to possibly extract forces and pressure distributions on such surfaces.

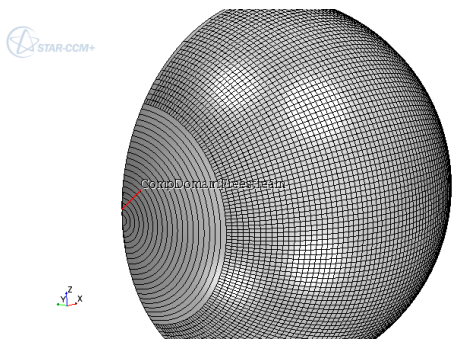

Figure 2.24: CFD domain 3D view

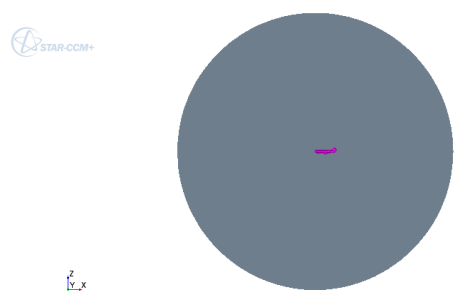

Figure 2.25: CFD domain 2D view with aircraft

To reduce the computational effort, only half of the whole aircraft has been modeled. This limits those computations on only symmetrical flow conditions, without the possibility of investigating roll and yaw flow conditions.

On the far field surface, a proper far field boundary condition has been applied, while a wall boundary condition has been applied on the aircraft surfaces.

The chosen turbulence model is the k-omega SST menter; this model works better than the Spalart-Allmaras when the AOA increases and larger separations are expected.

An unstructured mesh approach based on polyhedrons has been used: it allows a faster numerical convergence as compared with structured mesh, especially when the flow direction could change. This kind of mesh allows to change the angle of attack affecting little the solution. In this way the dissipative errors are reduced and there is no dependency on the flow direction. Attempts have been made to reduce as much as possible the skewness angle between cells with the goal of improving the

grid quality and reducing the mesh induced error.

To properly resolve the near wall boundary layer, a prism layer has been generated near the aircraft surfaces. The prism layer total thickness has been evaluated considering the associated Reynold number and simplified turbulent boundary layer thickness equation[13]: a total thickness of 0.003 m has been used. The prism layer distribution has included 15 layers starting from the distance of 1e-4m from the aircraft surfaces.

Two meshes with about 9 millions of cells (#1) and 15 millions of cells (#2) have been compared with very little difference in the aerodynamic coefficient evaluation. Hence, to reduce the computational demand, the #1 mesh has been used. Such mesh includes sufficient refinements where strong gradients are expected (e.i., wings, tail planes, gears, engines...). The used mesh is shown in Figure (2.26) and (2.27).

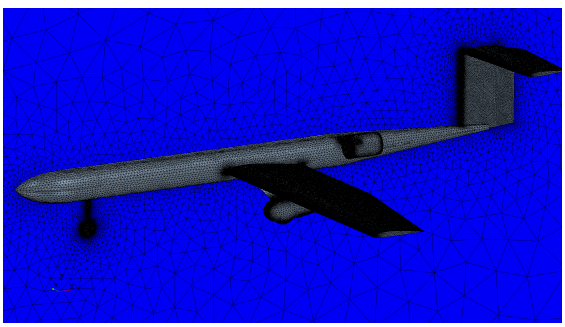

Figure 2.26: CFD mesh

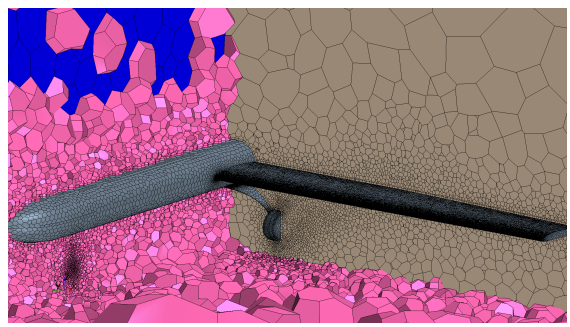

Figure 2.27: CFD mesh details

Figure (2.28) shows the pressure distribution on the whole aircraft at AOA = 0° and with Figure (2.29) it's possible to visualize the wake generated by the front gear and the stagnation point at the fuselage front.

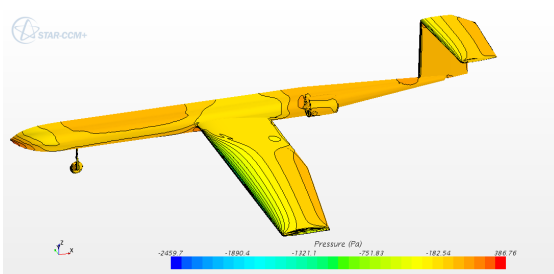

Figure 2.28: Pressure distribution on the whole aircraft at AOA = 0°

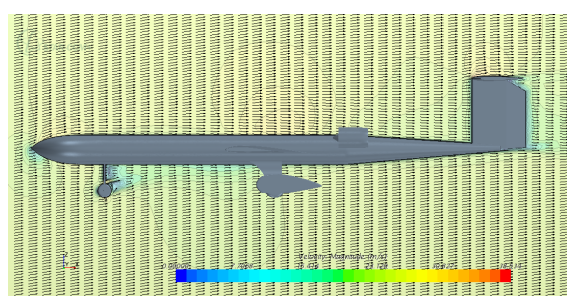

Figure 2.29: Htail airfoil - AOA=0°, $\delta_e = 0°$

The wall-y+ field function on the wall surfaces (Figure (2.30)) gives an idea of the mesh quality and of the approach used for resolving the boundary layer. Those values are acceptable for the level of accuracy required for this preliminary study.

Using the shear stress visualizations is possible to have an idea of the flow distribution on the wall, highlighting attached and separated flow areas. Figure (2.31) highlights the magnitude of the tip vortices around the wing and the horizontal tail tips. Also it shows how the flow near the wing tip is almost aligned with the far field velocity, whereas the flow near the fuselage junction is affected by the fuselage and the engine.

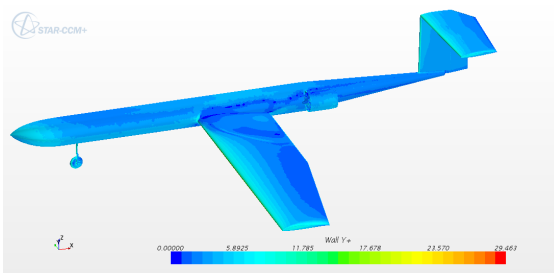

Figure 2.30: Wall-y+ field at AOA=0°

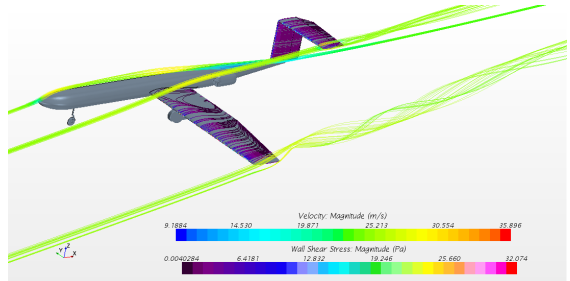

Figure 2.31: Streamlines and tip vortices visualization at AOA=10°

Figure (2.32) and (2.33) show the flow field around two foil sections of the wing and the horizontal tailplane respectively. From them, it's possible to identify the stagnation point and expansion area over the wing surface; also, it can be seen that at AOA = 0°, the flow separation around the foil is very limited. Differently, the horizontal tail flow field shows larger separation, even if the beneficial effect of the gap between the fixed and moving surfaces.

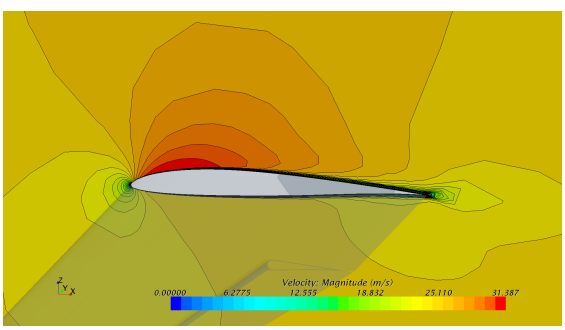

Figure 2.32: Wing airfoil - AOA=0°

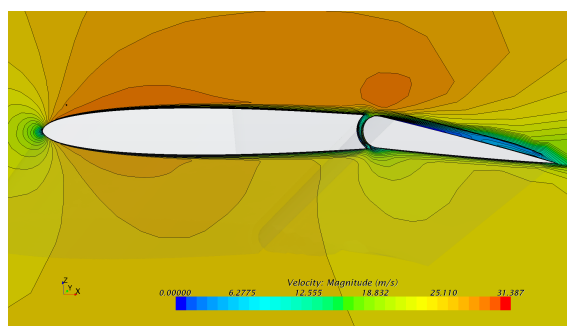

Figure 2.33: Htail airfoil - AOA=0°, $\delta_e = 10°$

The CFD simulations aim to evaluate lift, drag and moment coefficients in different flow (U, AOA) and elevator deflection conditions (δ_e). In this way, it possible to evaluate the coefficients derivatives as well. Each simulation has been run modifying one parameter at time, keeping the other fixed: i.e., the AOA simulations have been completed changing the AOAs from -5° to +5°, with a +2.5° step, keeping fixed the velocity U at 25 m/s and the δ_e to 0°. Similarly, the analyzed δ_e range is from -5° to +5°, with a + 2.5° step, whereas the three velocities, 20 m/s, 25 m/s and 30 m/s, have been considered.

Force coefficients are evaluated along the standard reference frame, with x axis in the horizontal (front-rear) direction, z axis in the vertical (upward) direction and, consequently, the y axis. Hence, being the aircraft fixed into the computational domain, it has been necessary to use equations (2.18) to transfer force coefficient from the standard reference frame to the wind axis:

$$C_N = C_L \sin\alpha + C_D \cos\alpha \tag{2.17}$$

$$C_T = C_D \cos\alpha - C_L \sin\alpha \tag{2.18}$$

Using these formulas, force coefficients have been evaluated for each investigated angle of attack. When AOA=0 deg, the lift and drag coefficients are directly the force coefficients along the x and z axis.

The elevator deflection causes stronger tip vortices around the horizontal tail tips, as seen near the wing tips. This vortices intensity increases with the amount of lift generated by the aerodynamic surface and, thus, they are weaker when the horizontal tail is unloaded (δ_e=0°). Such situation is also visible comparing Figure (2.34), (2.35), (2.36) and (2.37): the streamlines for the AOA = 0° and AOA = 10° show the increase of the roll-up motions near the aerodynamic surface tips, highlighting an higher pressure difference between the pressure and suction sides. Such larger pressure difference result in higher aircraft lift. Lastly, from them is possible to see that, increasing the AOA, the flow around the fuselage and other "passive" surfaces (that do not contribute in generating lift) tends to separate, resulting in an increased aircraft drag.

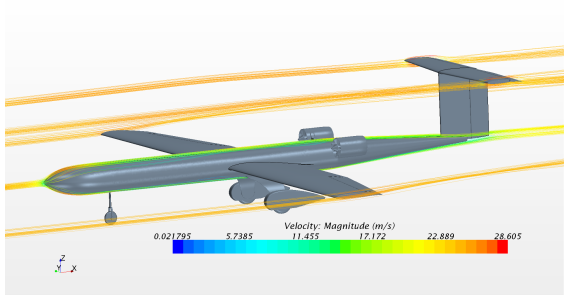

Figure 2.34: AOA=0°, $\delta_e = 10°$

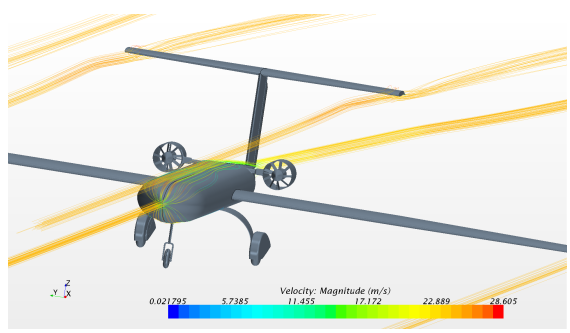

Figure 2.35: AOA=0°, $\delta_e = 10°$

The drag coefficients estimated are listed in the following Table 2.5.

2.3.1 Rough preliminary model validation

The purpose of this section, has been to verify, in the first istance, the correct input procedures used in the reference model comparing some estimated values with some other reliable method like

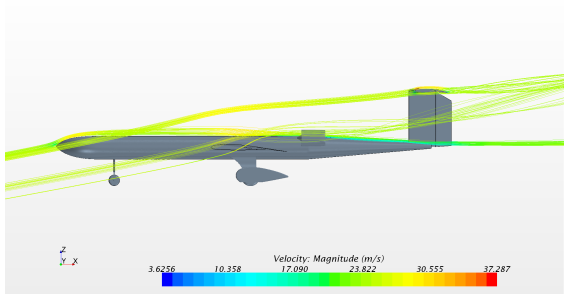

Figure 2.36: AOA=10°

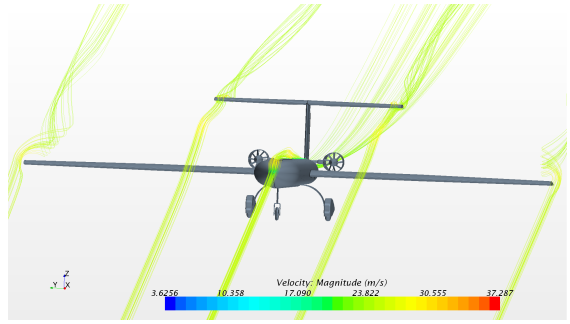

Figure 2.37: AOA=10°

Table 2.5: Drag coefficients estimated values

Aerodynamic CFD coefficients		
Drag coefficient for zero angle of attack	C_{D_0}	0.0470
Variation of drag coefficient with angle of attack	C_{D_α}	0.0024
Variation of drag coefficient with the body u-component velocity	C_{D_u}	0.0001
Variation of drag coefficient with elevator deflection angle	$C_{D_{\delta_e}}$	0.0078
Variation of lift coefficient with the body u-component velocity	C_{L_u}	$6 \cdot 10^{-5}$
Variation of pitching moment coeff. with the body u-component velocity	C_{m_u}	$2 \cdot 10^{-5}$

DATCOM and an other VLM software. In particular, in order to perform a model validation of the reference model, few coefficients have been roughly estimated with System Identification after performing flight testing.

A semi-empirical method as Athena Vortex Lattice (AVL) [14] have been used to check the magnitude range validity of some aerodynamic coefficient like C_{L_α}, C_{M_α}, C_{M_q} C_{L_q}. The United State Air Force stability and control DATCOM[15] method, that relies solely on aircraft geometrical and mass properties and is therefore simpler to realize, has only been used tio create the 3D model for the flight simulator; in fact, this approach, cannot provide reliable results at such low speed. Figure (2.38) and (2.39) show the Datcom model developed while Figure (2.40) and (2.41) show the AVL model with trailing edge visualization, normal forces and pressure distribution.

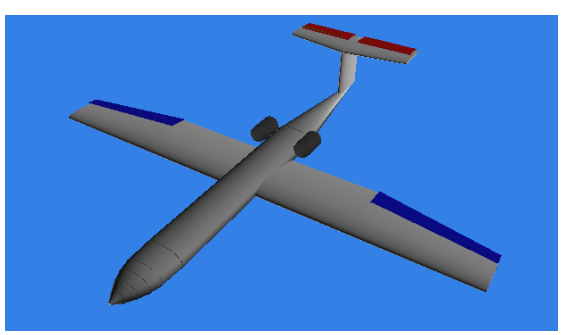

Figure 2.38: 3D Datcom model

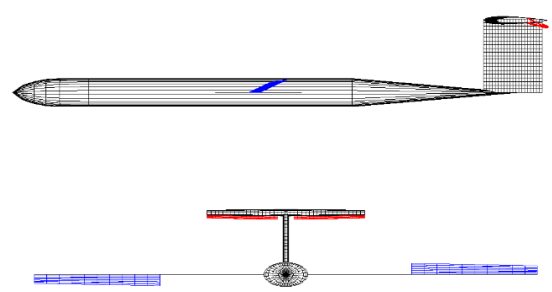

Figure 2.39: 3D Datcom model views plotted with a DATCOM Pro+ Matlab script

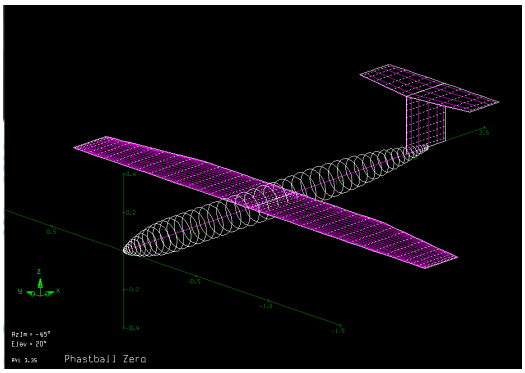

Figure 2.40: AVL model geometry

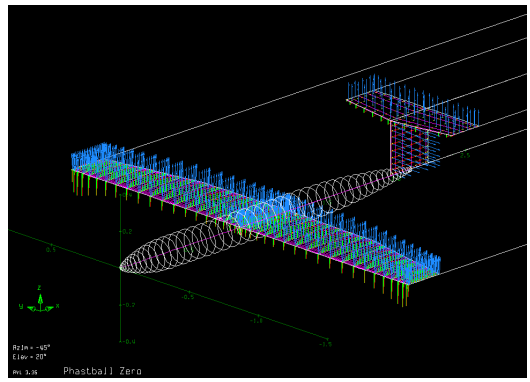

Figure 2.41: AVL model visualizations

2.4 Model-Aided Navigation Architecture

The architecture of the algorithm used in this work consists of two subsystems: the first is related to the INS that estimates position, velocity and attitude of the aircraft using the IMU data while the second the VDM which also estimates velocity and attitude through the equation of motion and estimated forces and movements based on the coefficients from VLM.

2.4.1 Vehicle Dynamic Model

For the VDM section, in order to estimate velocity and attitude, the equations of motion cited in 2.2.2 are used.

The force and moment coefficients have been calculated in the form

$$C_L = C_{L_0} + C_{L_\alpha}\alpha + C_{L_u}\left(\frac{u}{V}\right) + C_{L_q}\left(\frac{c}{2V}\right)q + C_{L_{\delta_e}}\delta_e \tag{2.19}$$

$$C_D = C_{D_0} + \frac{1}{\pi e_0 \text{Æ}} C_L^2 + C_{D_\alpha}\alpha + C_{D_u}\left(\frac{u}{V}\right) + C_{D_{\delta_e}}\delta_e \tag{2.20}$$

$$C_Y = C_{Y_\beta}\beta + C_{Y_p}\left(\frac{b}{2V}\right)p + C_{Y_r}\left(\frac{b}{2V}\right)r + C_{Y_{\delta_a}}\delta_a + C_{Y_{\delta_r}}\delta_r \tag{2.21}$$

$$C_l = C_{l_\beta}\beta + C_{l_p}\left(\frac{b}{2V}\right)p + C_{l_r}\left(\frac{b}{2V}\right)r + C_{l_{\delta_a}}\delta_a + C_{l_{\delta_r}}\delta_r \tag{2.22}$$

$$C_M = C_{M_0} + C_{M_\alpha}\alpha + C_{M_u}\left(\frac{u}{V}\right) + C_{M_q}\left(\frac{c}{2V}\right)q + C_{M_{\delta_e}}\delta_e + C_L\left(\frac{\delta_{\text{cg}}}{c}\right) \tag{2.23}$$

$$C_N = C_{N_\beta}\beta + C_{N_p}\left(\frac{b}{2V}\right)p + C_{N_r}\left(\frac{b}{2V}\right)r + C_{N_{\delta_a}}\delta_a + C_{N_{\delta_r}}\delta_r \tag{2.24}$$

$$C_X = C_D \sin\alpha - C_L \cos\alpha \tag{2.25}$$

$$C_Z = -C_D \cos\alpha - C_L \sin\alpha \tag{2.26}$$

In the previous equations, $\bar{c}$ is the wing chord, α is the angle of attack, β is the sideslip angle, e_0 is the Oswald efficiency number, $\boldsymbol{Æ}$ is the aspect ratio, b is the wing span, V is the total velocity, u is the forward speed, δ is referred to the aileron, elevator and rudder deflections, $\dot{\alpha}$ is the aerodynamic-angle rate, and p,q and r are the components of the aircraft body-axis angular-velocity vector.

2.4.2 Inertial Navigation System

For the INS, the mechanization derived in Groves (2013) [16] for positioning in a Earth frame with NED velocity and attitude. In order to calculate position (p_n), velocity (v_n) and Euler angles (Φ) in the North-East-Down (NED) frame n, the following equations are used,

$$\dot{p} = v_n \tag{2.27}$$

$$\dot{v} = C_b^n f_b + g_n - (\Omega_{en}^n + 2\Omega_{ie}^n) v_n \tag{2.28}$$

$$\dot{\Phi} = E_b^n w_b \tag{2.29}$$

where C_b^n is the body to navigation frame transformation matrix, f_b is the body-axis specific force vector, E_b^n is the rotation rate transformation matrix, and w_b is the body-axis angular rate vector.

The third term of Equation (2.28) takes into account of the Earth's rotation considering the following terms.

$$\Omega_{en}^n = \begin{bmatrix} 0 & -\omega_{en,z}^n & \omega_{en,y}^n \\ \omega_{en,z}^n & 0 & -\omega_{en,x}^n \\ -\omega_{en,y}^n & \omega_{en,x}^n & 0 \end{bmatrix} \tag{2.30}$$

$$\omega_{en}^n = \begin{bmatrix} v_{eb,E}^n/(R_E(L_b) + h_b) \\ -v_{eb,N}^n/(R_N(L_b) + h_b) \\ (-v_{eb,E}^n \tan L_b)/(R_E(L_b) + h_b) \end{bmatrix} \tag{2.31}$$

$$\Omega_{ie}^{n} = \omega_{ie} \begin{bmatrix} 0 & \sin L_b & 0 \\ -\sin L_b & 0 & -\cos L_b \\ 0 & \cos L_b & 0 \end{bmatrix} \tag{2.32}$$

Furthermore, knowing that $\omega_{ie} = 7.29212\,\mathrm{rad/s^{-1}}$ is the WGS 84 Earth's angular rotationrate and,

$$R_N(L_b) = \frac{R_0(1-e^2)}{(1-e^2\sin^2 L_b)^{3/2}} \tag{2.33}$$

$$R_E(L_b) = \frac{R_0}{\sqrt{(1-e^2\sin^2 L_b)}} \tag{2.34}$$

where R_N is the radius of curvature for North-South motion, R_E is the radius of curvature for East-West motion, $R_0 = 6378137\,\mathrm{m}$ is the equatorial radius, $e = 0.0818191918425$ is the eccentricity, and L_b is the geodetic latitude.

2.4.3 Filter Design

Figure 2.42 illustrate the configuration used in the proposed approach.

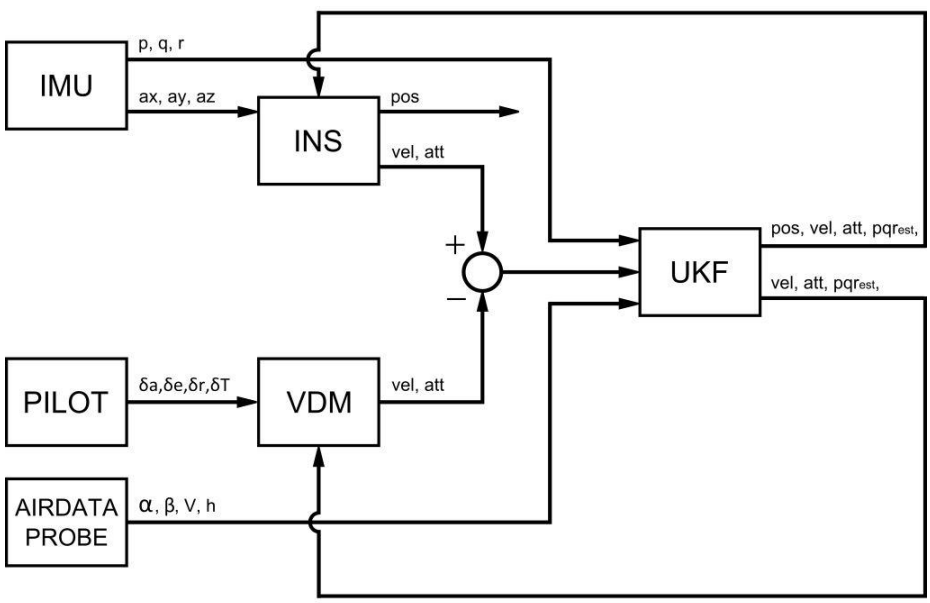

Figure 2.42: Model-Aided Navigation configuration.

As shown in Figure 2.42, an Unscented Kalman filter (UKF)[17],[18],[19] is used to fuse the outputs from INS and the VDM. For details on how to implement the UKF algorithm, the reader is

turned to [20], in this section, the key elements of of the UKF used in this work including the state vector, $\mathbf{x}$, nonlinear prediction model, f, measurement update model, h, and assumed process noise, Q and measurement noise, R, are outlined .

The state vector $\mathbf{x}$ consists of the following 12 states (position, velocity, body-to-NED Euler angles, and estimated angular rates $[p, q, r]$):

$$\mathbf{x} = [\, x \;\; y \;\; z \;\; V_N \;\; V_E \;\; V_D \;\; \phi \;\; \theta \;\; \psi \;\; p \;\; q \;\; r \,]$$

At each time step k, the unscented transformation is used to generate a set of sigma-points using the previous epoch, $k-1$, estimated state and error-covariance. Then, state estimates are propagated in time using the INS formulation described in Section 2.4.2, denoted as f.

$$x_k = f(x_{k-1}, e_{k-1}, p_{k-1}) + w_{k-1} \tag{2.35}$$

It should be noted since the aircraft body-axis rates are included as an estimated states, that these estimated p, q and r are used within the INS mechanism for attitude prediction as opposed to the IMU measured values. Furthermore, these states are predicted as a random-walk process by adding process noise. Next, for the measurement update, h, the same set of sigma points that are used for predicting with INS are within the aircraft vehicle dynamic model (VDM) as described in Section 2.4.1 are differenced with the INS predictions to form pseudo-measurements.

$$y_k = h(x_k, e_k, p_k) + v_k \tag{2.36}$$

In particular, the attitude and velocity predicted with INS within Eq. 2.35 and the attitude and velocity predicted with VDM are differenced within Eq. 2.36, such that, with an ideal INS and ideal VDM a pseudo-measurement can be used to take advantage of the information that these difference should be 0. These 6 "pseudo-measurements" are combined with the IMU measured angular rates p, q and r, such that there are 9 measurements in the baseline model added navigation configuration.

$$z_k = \begin{bmatrix} 0_{1x6} & p_{IMU} & q_{IMU} & r_{IMU} \end{bmatrix} \tag{2.37}$$

Where the 6 zeros account for the "pseudo-measurement" constraints, and the angular rate states are directly observed by the IMU,

In addition to these nine baseline measurements, the addition of a three airspeed sensor and one

altimeter were also considered as additional configurations. The airspeed and altimeter measurement update equations included within h, when utilized are shown in Equation (2.38) to (2.41),

$$u_{\mathrm{m}} = V \cos(\alpha) \cos(\beta) \tag{2.38}$$

$$v_{\mathrm{m}} = V \sin(\beta) \tag{2.39}$$

$$w_{\mathrm{m}} = V \sin(\alpha) \cos(\beta) \tag{2.40}$$

$$a_{\mathrm{m}} = h + \eta \tag{2.41}$$

where V is the measured airspeed, h is the measured altitude and η is the altimeter measurement noise.

In 2.36, $\hat{X}_k$ is the updated state at time step k, $\hat{x}_{k|k-1}$ is the predicted state at time step k from (2.35), and $\hat{y}_{k|k-1}$ is the predicted output at time step k from (2.35).

Chapter 3

Experimental setup

3.1 Flight Simulation

A 6Dof Flight Simulator has been developed using Simulink to get all the required data to make the MAN architectures work. The aircraft motion has been modeled using the linear model cited in the previous chapter, the force and moment equations with a custom block that use the standard formulations and the equations of motion solved with the Simulink 6DoF (Euler Angles) blockset. The following Simulink blocksets have been used too:

- COESA Atmosphere Model (For Temperature, Speed of Sound, Pressure and Air Density)
- Incidence, Sideslip & Airspeed
- Dynamic Pressure
- WGS84 Gravity Model

The wind has been modeled using the following blocksets:

- Dryden Wind Turbulence Model (Continuous (+q -r))
- Discrete Wind Gust Model
- Dynamic Pressure
- Wind Shear Model

Additionally the three-axis inertial measurement unit has been used to simulate the IMU measurements.

The Flight Simulator can be controlled by a joystick or by a Matlab script containing the pilot commands. This script control feature is contained in the main input script file that contains the aircraft aerodynamic coefficients, mass and inertia properties; this same script is able trough a variable to consider or not windy conditions and eventually to modify the wind input parameters. In-board sensors as Pitot and Vanes are simulated perturbing the 6Dof solutions with random noise and errors. All the available output variables are then stored in a single data files labeled according the actual date. Five-minutes length flights has been performed with this simulator in order to imitate the real flights.

An open source flight interface, FlightGear [21], as been used to actually visualize the simulated trajectories as shown in Figure (3.1).

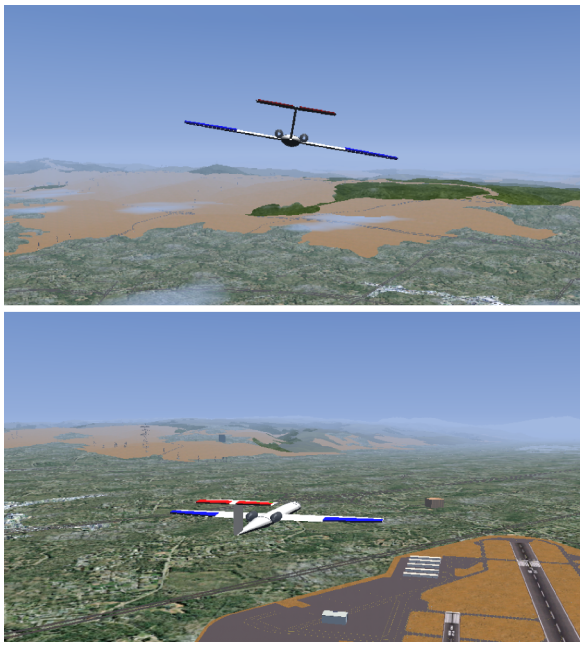

Figure 3.1: FlighGear interface

3.2 Flight Testing

All flight testing sessions have been conducted at the Louis Bennett Field (FAA LID: WV23), shown in Figure (3.2). This field is a West Virginia University owned private-use airport located in Lewis County, West Virginia. It has an elevation of 309 m above mean sea level and one asphalt paved runway which measures 974 x 15 m.[22]

The Flight testing sessions consider the aircraft balancing at first. The testbed is balanced considering the aircraft CG positioned at the 25% of the mean aerodynamic chord.

Figure 3.2: Louis Bennet Field satellite image (source: Google Maps)

Flight testing sessions are performed by expert pilots and last generally five minutes (due to engine batteries capabilities). The take off direction is usually in the south direction and, of course, anyway toward the wind direction. The average flight altitude is 100 m above the ground level. Figure (3.3) and Figure (3.4) show a tail camera screenshot and a down looking image respectively.

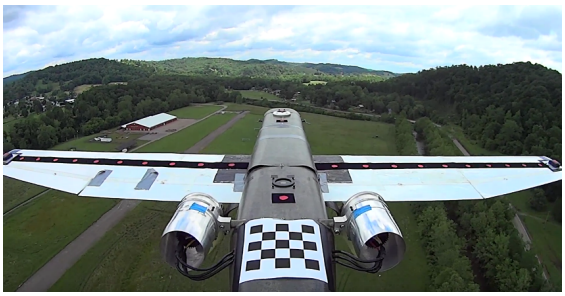

Figure 3.3: Tail camera image during flight testing

Figure 3.4: Down looking camera image during flight testing

Figure (3.5) shows the typical ground track trajectories and Figure (3.6) the flight used in the following Chapter.

The IMU platform cited in the Testbed section, collect the 3-axis acceleration, angular rates and magnetometer data. The nose GPS module allows the estimation of the ECEF position and subsequently, using a 15-states loosely-coupled GPS/INS EKF filter [18][19], the relative Euler Angles and all the other flight results needed for the MAN architectures.

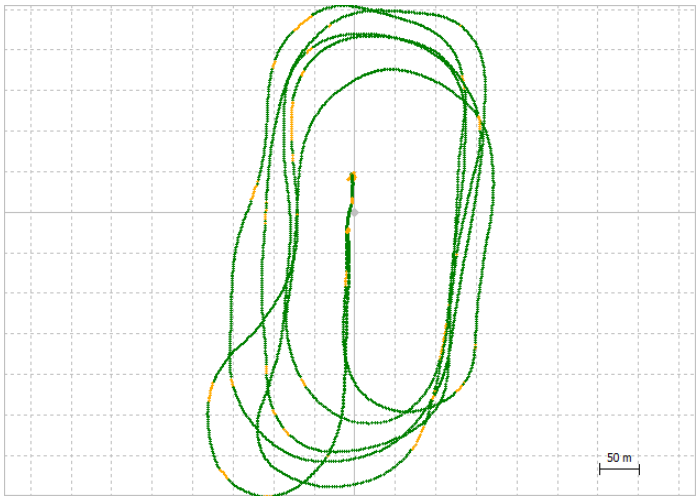

Figure 3.5: Ground track

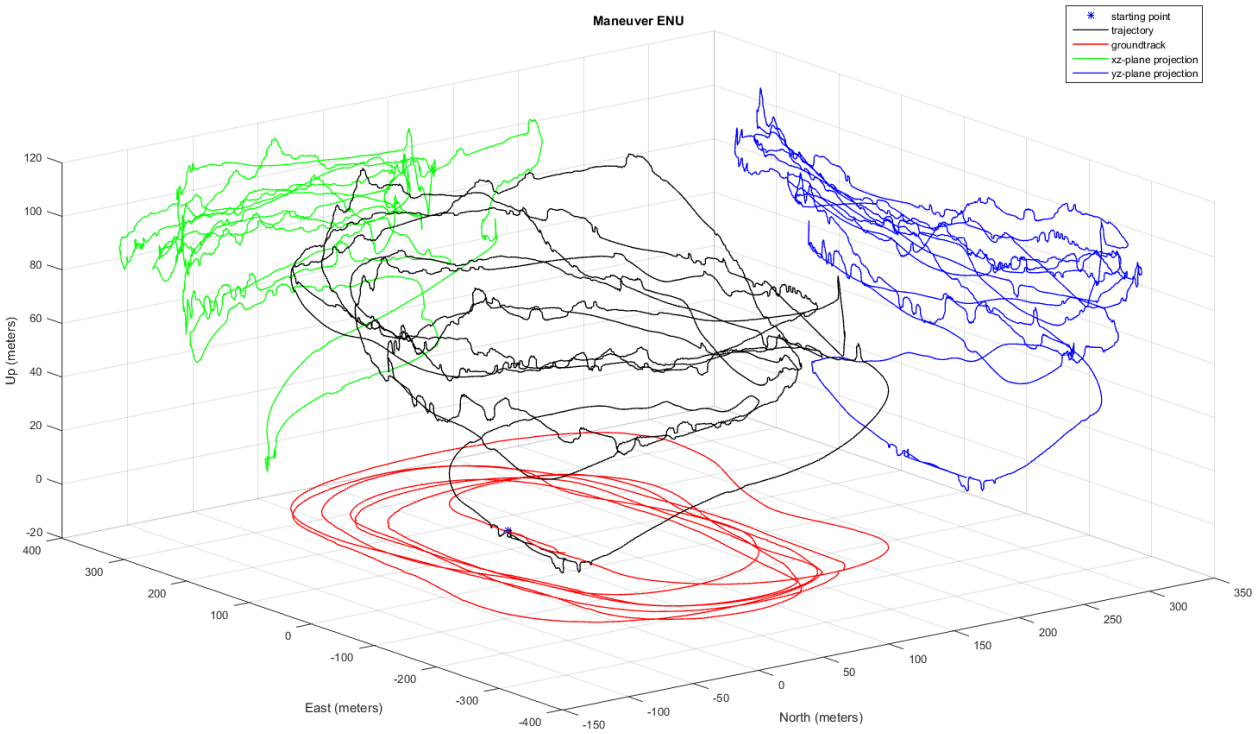

Figure 3.6: Flight testing trajectories

Chapter 4

Results

Parts of this chapter are taken from the conference paper "Sensitivity of Unmanned Aerial Vehicle Model-Aided Navigation"[7]

4.1 Flight Simulation

To assess performance sensitivity, the aircraft localization results are computed with the following conditions varied:

- Model-aided navigation architecture (i.e., inclusion of airspeed and altimeter measurements);
- IMU sensor grade (i.e., ranging from automotive to tactical grade);
- UAV dynamic model quality with respect to truth (i.e., perturbing the modeled coefficients with errors).

All results are expressed in terms of velocity and altitude drift for the INS alone and integrated navigation approach.

The 12×12 process noise covariance matrix Q and the 9×9 to 13×13 (depending on the architecture chosen) measurement noise covariance matrix R values for the Flight Simulation data are expressed in Table 4.1.

Table 4.1: Process noise covariance matrix Q and measurement noise covariance matrix R values for Flight Simulation data.

Process noise covariance matrix Q	Position	$5.6 \cdot 10^{-8}$ rad
	Velocity	$8 \cdot 10^{-4}$ m/s
	Attitude	$3.05 \cdot 10^{-8}$ rad
	Angular Rates	$3.05 \cdot 10^{-6}$ rad/s
Measurement noise covariance matrix R	Velocity	1 m/s
	Attitude	1 rad
	Angular Rates	1 rad/s
	Airspeed	2 m/s
	Altimeter	1 m

4.1.1 Model-aided navigation architecture

First, the three different architectures were considered, depending on the measurement technique adopted as mentioned above, namely:

- VDM-aiding only
- VDM with airspeed measurements
- VDM, with airspeed and altimeter measurements

As shown in Table 4.2, introducing the airspeed sensor we obtain better results in terms of position, velocity and attitude. The introduction of the altimeter further improves the positioning performance.

As an example, Figure (4.1), Figure (4.2) and Figure (4.3) show an example of the results obtained for a single case. It is important to note that in all the three architectures, in most respects, the MAN approach results to perform better than the INS alone. That is, velocity and attitude are always better, and overall positioning is typically better.

4.1.2 IMU sensor grade

Next, in order to assess the sensitivity to IMU grade, different scaled versions of the reference IMU listed in Table 4.3, have been created in order to simulate various sensor grades.

The results are contained in the Table 4.4.

As indicated, as expected, the performance typically increases in terms of position and attitude estimation using a better IMU above all switching from IMU#1 scaling factor of 50 times worse than IMU#2, which represents an automotive grade IMU to IMU#2 (Baseline tactical grade IMU), to IMU#3 which has a scaling factor of 1/1000 with respect to IMU#2, which is representative of

			Position (m)	Velocity (m/s)	Attitude (deg)
Flight #1		INS	2857.34	26.26	1.28
	VDM only	MAN	3812.93 (-33%)	10.73 (93%)	0.78 (39%)
	VDM + Airsp	MAN	2221.26 (22%)	0.26 (99%)	0.73 (43%)
	VDM + Airsp + Alt	MAN	2201.64 (23%)	0.26 (99%)	0.74 (42%)
Flight #2		INS	1964.83	26.26	1.28
	VDM only	MAN	3503.28 (-78%)	10.62 (59%)	0.83 (35%)
	VDM + Airsp	MAN	3503.28 (-78%)	10.62 (59%)	0.83 (35%)
	VDM + Airsp + Alt	MAN	1637.57 (17%)	0.25 (99%)	0.75 (41%)
Flight #3		INS	5761.41	25.85	1.21
	VDM only	MAN	2786.2 (52%)	12.12 (53%)	0.89 (26%)
	VDM + Airsp	MAN	2823.94 (51%)	0.25 (99%)	0.72 (40%)
	VDM + Airsp + Alt	MAN	2704.73 (53%)	0.25 (99%)	0.72 (40%)
Flight #4		INS	5534.09	25.82	1.22
	VDM only	MAN	4489.31 (19%)	11.25 (56%)	0.82 (33%)
	VDM + Airsp	MAN	3728 (33%)	0.26 (99%)	0.72 (41%)
	VDM + Airsp + Alt	MAN	3709.81 (33%)	0.26 (99%)	0.73 (40%)
Flight #5		INS	5604.81	25.79	1.24
	VDM only	MAN	2919.03 (48%)	11.8 (54%)	0.84 (32%)
	VDM + Airsp	MAN	2755.16 (51%)	0.26 (99%)	0.71 (43%)
	VDM + Airsp + Alt	MAN	2650.9 (53%)	0.26 (99%)	0.71 (43%)

Table 4.2: Model-Aided Navigation architectures results

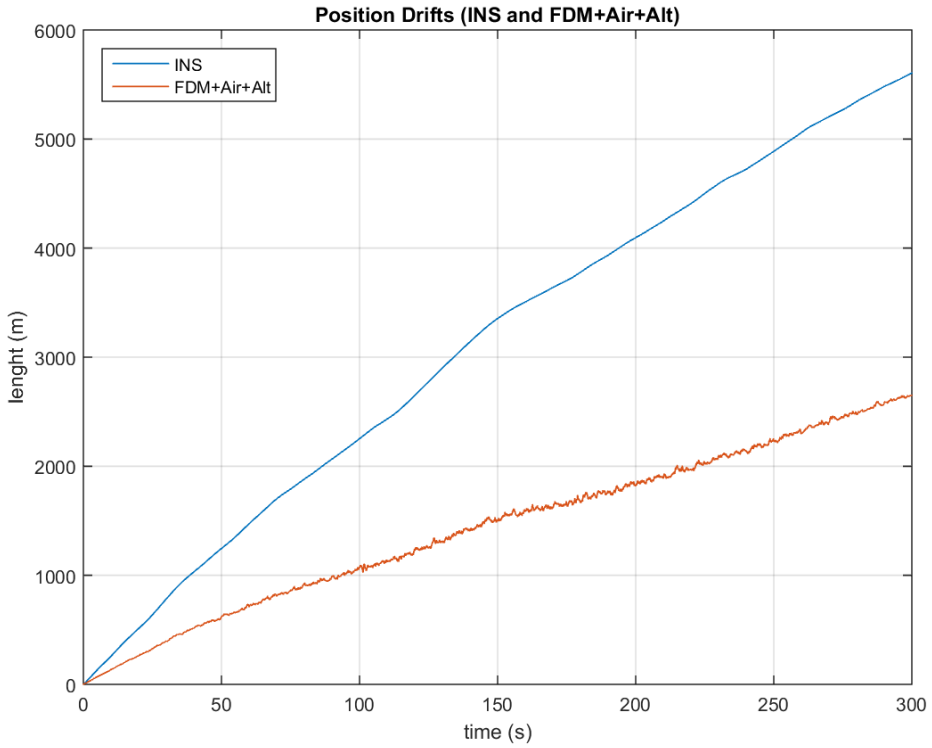

Figure 4.1: Position drifts related to the VDM

an intermediate grade IMU. However, this trend is not a severe for MAN approaches. That is, the performance remains fairly consistent for positioning, even as the IMU degrades.

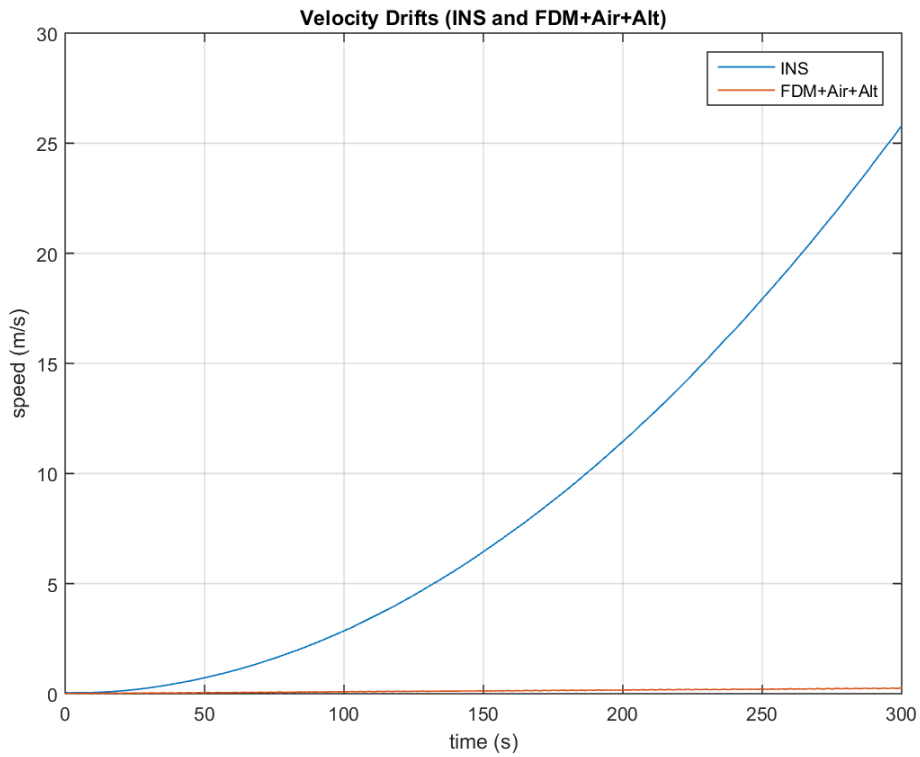

Figure 4.2: Velocity drifts related to the VDM

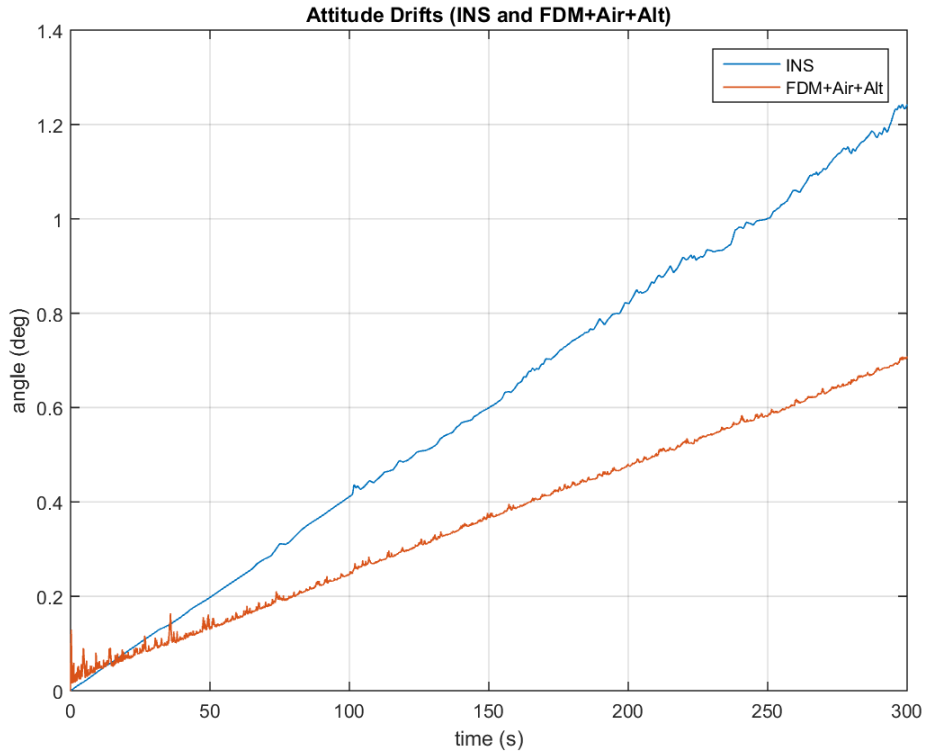

Figure 4.3: Attitude drifts related to the VDM

Table 4.3: Honeywell HG1930BA50 Performance [23]

Gyro Bias Repeatability	40 °/h 1σ
Gyro Bias In-run Stability	1.5kg
Angular Random Walk (ARW)	0.09^5, 0.09^5 °/$\sqrt{\text{h}}$ max
Accel Bias Repeatability	10 mg 1σ
Accel Bias In-run Stability	0.5kg 1σ
Velocity Random Walk (VRW)	0.3 ps/$\sqrt{\text{h}}$ max

Table 4.4: IMU sensor grades' results

			Position (m)	Velocity (m/s)	Attitude (deg)
Flight #1	IMU #1	INS	6110.55	56.59	1.66
		MAN	2046.08 (66%)	0.18 (99%)	0.51 (69%)
	IMU #2	INS	2765.61	25.98	1.27
		MAN	2222.51 (19%)	0.26 (99%)	0.74 (42%)
	IMU #3	INS	2857.34	26.26	1.28
		MAN	2201.64 (23%)	0.26 (99%)	0.74 (42%)
Flight #2	IMU #1	INS	4691.24	63.5	1.41
		MAN	1704.47 (64%)	0.18 (99%)	0.8 (43%)
	IMU #2	INS	2017.02	25.42	1.27
		MAN	1605.4 (20%)	0.26 (99%)	0.76 (40%)
	IMU #3	INS	1964.83	26.26	1.28
		MAN	1637.57 (17%)	0.25 (99%)	0.75 (41%)
Flight #3	IMU #1	INS	9159.58	134.04	4.12
		MAN	68576.87 (-648%)	0.45 (99%)	1.37 (66%)
	IMU #2	INS	5785.67	25.8	1.21
		MAN	2706.4 (53%)	0.25 (99%)	0.71 (41%)
	IMU #3	INS	5761.41	25.85	1.21
		MAN	2704.73 (47%)	0.25 (99%)	0.72 (40%)
Flight #4	IMU #1	INS	7096.55	54.53	1.91
		MAN	3729.55 (47%)	0.27 (99%)	0.75 (61%)
	IMU #2	INS	5536.89	25.66	1.22
		MAN	3741.62 (32%)	0.27 (99%)	0.74 (39%)
	IMU #3	INS	5533.96	25.82	1.22
		MAN	3709.81 (33%)	0.26 (99%)	0.73 (40%)
Flight #5	IMU #1	INS	6253.95	28.03	2.48
		MAN	52791.34 (-744%)	0.74 (97%)	2.19 (11%)
	IMU #2	INS	5436.11	26.63	1.27
		MAN	2664.19 (51%)	0.27 (99%)	0.73 (42%)
	IMU #3	INS	5604.69	25.8	1.24
		MAN	2650.9 (53%)	0.26 (99%)	0.71 (43%)

4.1.3 UAV dynamic model quality with respect to truth

Finally, the sensitivity to the quality of the aerodynamic model was also investigated by perturbing the value of the model coefficients with 10% and 20% error, respectively. These perturbation values are merely optimistic assumptions; Modeling errors can be much higher (for instance referring to the drag coefficient values, usually the most difficult to estimate).

Within Table 4.5 the attitude estimate that appears to not be influenced by these variations, however, the position difference gets worse with deteriorating aerodynamic model. However, even at the worst evaluated condition of 20% modeling errors, the integrated navigation is still better than the INS alone. As an example, these results are shown for a single fight, within Figure (4.4) and Figure (4.5).

Table 4.5: UAV dynamic model quality results

			Position (m)	Velocity (m/s)	Attitude (deg)
Flight #1		INS	2857.34	26.26	1.28
	truth	MAN	3812.93 (-33%)	10.73 (59%)	0.78 (39%)
	truth + 10%	MAN	4298.88 (-50%)	12.75 (51%)	0.77 (68%)
	truth + 20%	MAN	4691.39 (-64%)	14.34 (45%)	0.77 (68%)
Flight #2		INS	1964.83	26.26	1.28
	truth	MAN	3503.28 (-78%)	10.62 (59%)	0.83 (35%)
	truth + 10%	MAN	4035.03 (-105%)	12.58 (52%)	0.82 (36%)
	truth + 20%	MAN	4456.09 (-126%)	14.12 (46%)	0.81 (37%)
Flight #3		INS	5761.41	25.85	1.21
	truth	MAN	2786.2 (52%)	12.12 (53%)	0.89 (26%)
	truth + 10%	MAN	4936.7 (14%)	15.17 (41%)	0.87 (28%)
	truth + 20%	MAN	4936.7 (14%)	15.17 (41%)	0.87 (28%)
Flight #4		INS	5534.09	25.82	1.22
	truth	MAN	4489.31 (19%)	11.25 (56%)	0.82 (33%)
	truth + 10%	MAN	4758.01 (14%)	13.24 (48%)	0.82 (33%)
	truth + 20%	MAN	4990.07 (10%)	14.79 (43%)	0.83 (32%)
Flight #5		INS	5604.81	25.79	1.24
	truth	MAN	2919.03 (48%)	11.8 (54%)	0.84 (32%)
	truth + 10%	MAN	3940.19 (30%)	13.57 (47%)	0.83 (33%)
	truth + 20%	MAN	5091.48 (10%)	14.97 (42%)	0.83 (33%)

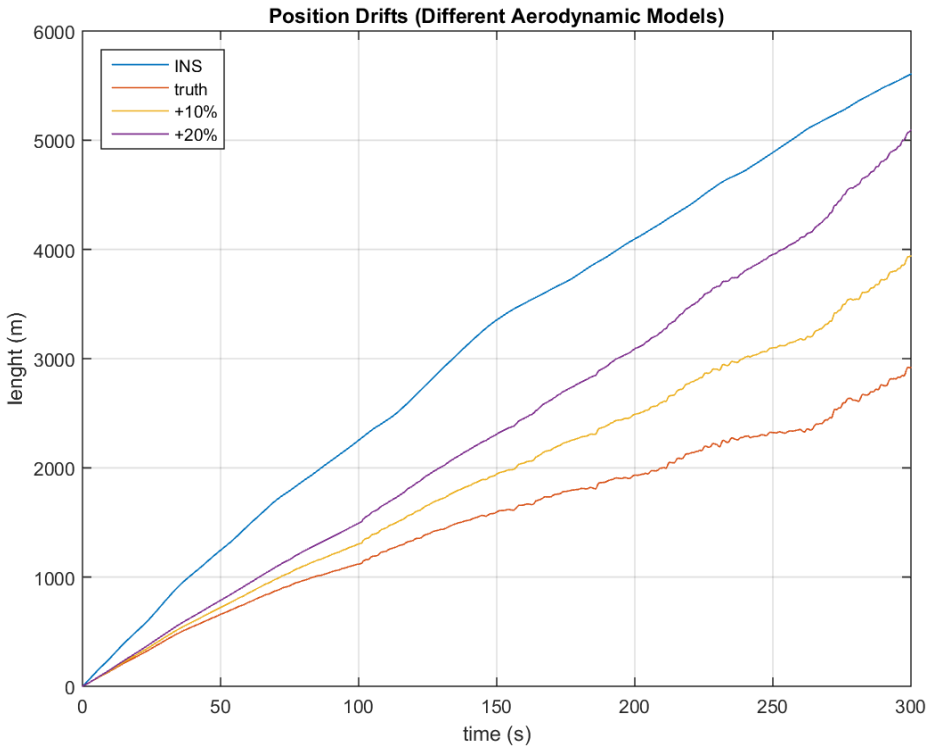

Figure 4.4: Position drifts related to the different aerodynamic models

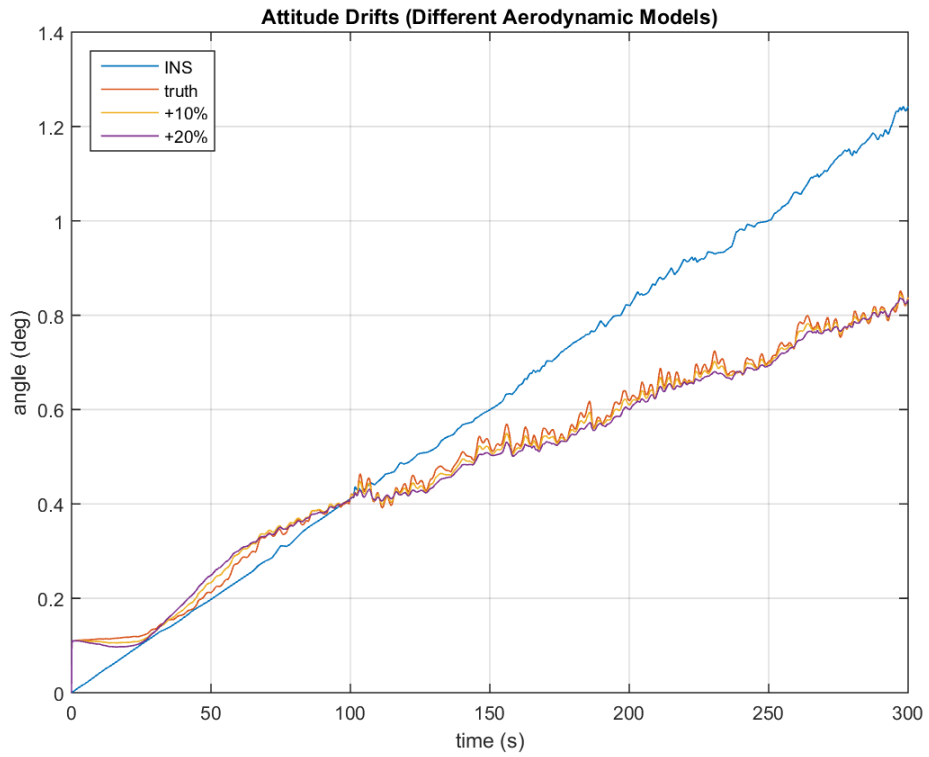

Figure 4.5: Attitude drifts related to the different aerodynamic models

4.2 Flight Testing

4.2.1 Model-Aided navigation architecture

As for the simulated data, the three different architectures were considered for the flight testing data, depending on the measurement technique adopted, namely:

- VDM-aiding only
- VDM with airspeed measurements
- VDM, with airspeed and altimeter measurements

The same dimensions process noise covariance matrix Q and measurement noise covariance matrix R values for the Flight Testing data are expressed in Table 4.6.

Table 4.6: Process noise covariance matrix Q and measurement noise covariance matrix R values for Flight Testing data.

Process noise covariance matrix Q	Position	$5.6 \cdot 10^{-8}$ rad
	Velocity	$8 \cdot 10^{-4}$ m/s
	Attitude	$2.98560 \cdot 10^{-18}$ rad
	Angular Rates	0.01290 rad/s
Measurement noise covariance matrix R	Velocity	1 m/s
	Attitude	1 rad
	Angular Rates	1 rad/s
	Airspeed	4 m/s
	Altimeter	4 m

As shown in Table 4.8, introducing the airspeed sensor we obtain better results in terms of position and velocity and the introduction of the altimeter further improves only the velocity performance.

Figure (4.6), Figure (4.7) and Figure (4.8) shows an example of the results obtained considering the INS+VDM architecture. Figure (4.9), Figure (4.10) and Figure (4.11) shows an example of the results obtained considering the INS+VDM+Airspeed architecture. Figure (4.12), Figure (4.13) and Figure (4.14) shows an example of the results obtained considering the INS+VDM+Airspeed+Altimeter

Table 4.7: Model-Aided Navigation architectures results

			Position (m)	Velocity (m/s)	Attitude (deg)
Flight #1		INS	821586.4	5320.7	57.3
	VDM only	MAN	605566.9	4770.8	180.5
	VDM + Airsp	MAN	184731.9	22.0	231.2
	VDM + Airsp + Alt	MAN	784092.3	18.3	222.2

Table 4.8: Model-Aided Navigation architectures results

		Position (m)	Velocity (m/s)	Attitude (deg)
VDM only	INS	821586.4	5320.7	57.3
	MAN	655359.5	5127.7	38.4

architecture architecture.

For the flight testing data, the Q and R value cited in the previous chapter make, in all the three architectures, the MAN approach results to perform better than the INS alone in terms of position and velocity.

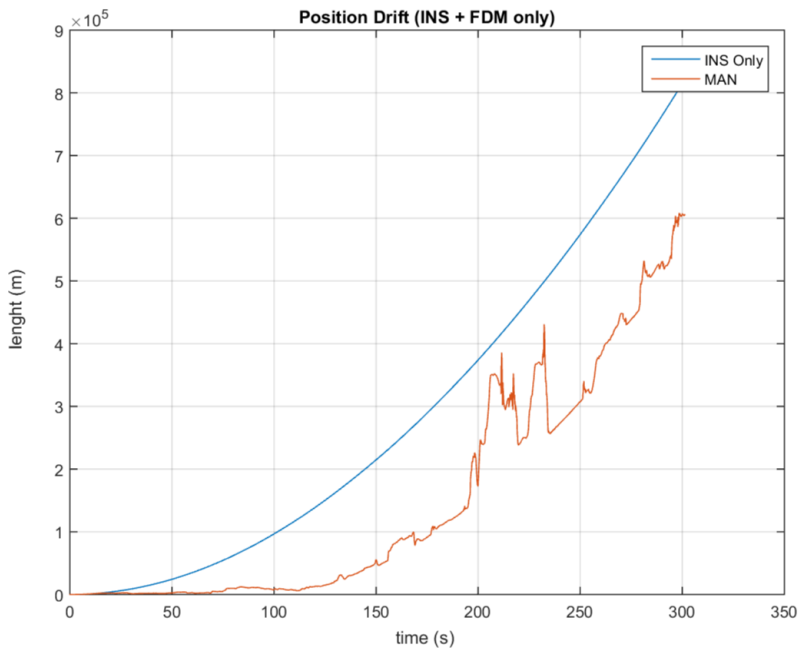

Figure 4.6: Position drifts related of INS alone and MAN (INS+VDM architecture)

It is has been possible to check that different values of Q and R anyway, made all the MAN approach results better in terms of position, velocity and attitude at least for the INS+VDM only architecture as shown in Figure (4.15), Figure (4.16) and Figure (4.17).

The Q and R values used in the last case are listed in Table (4.9 on page 47).

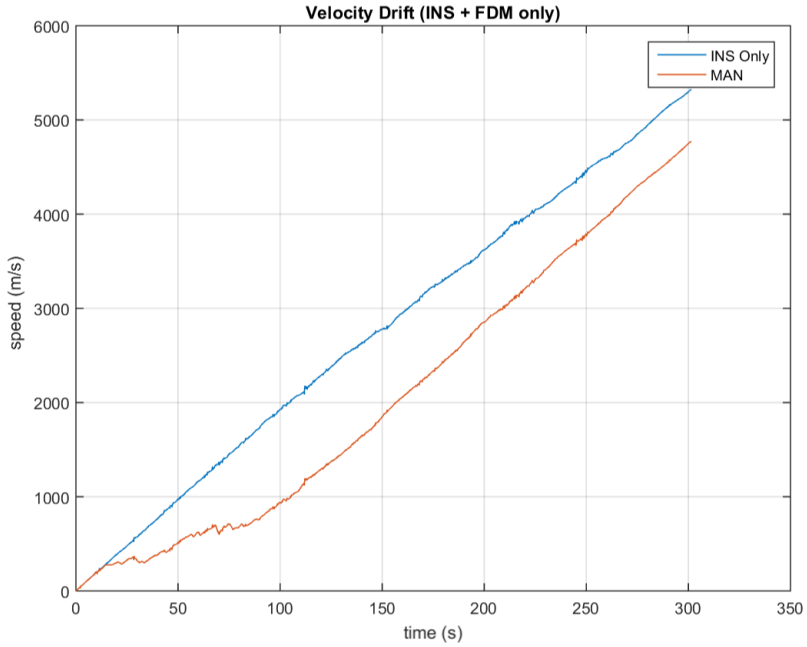

Figure 4.7: Velocity drifts related of INS alone and MAN (INS+VDM architecture)

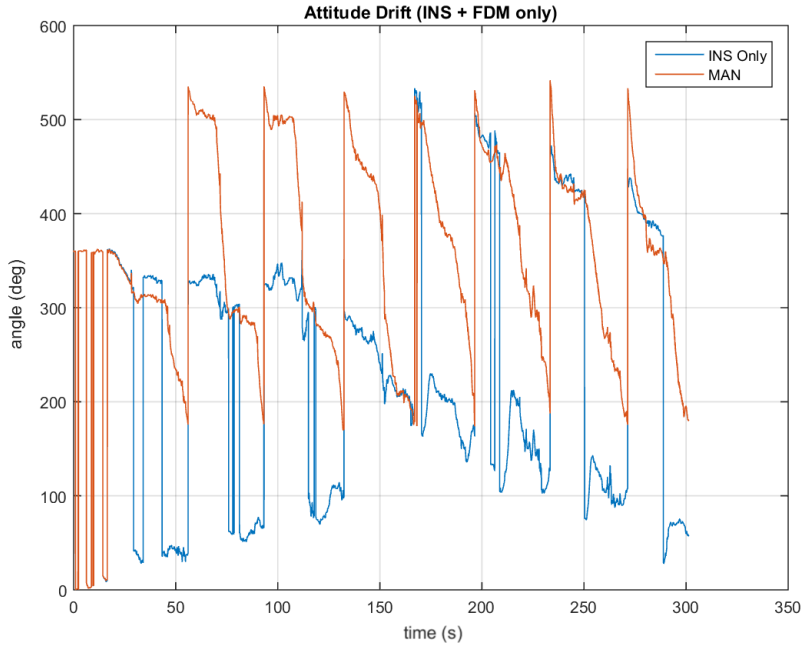

Figure 4.8: Attitude drifts related of INS alone and MAN (INS+VDM architecture)

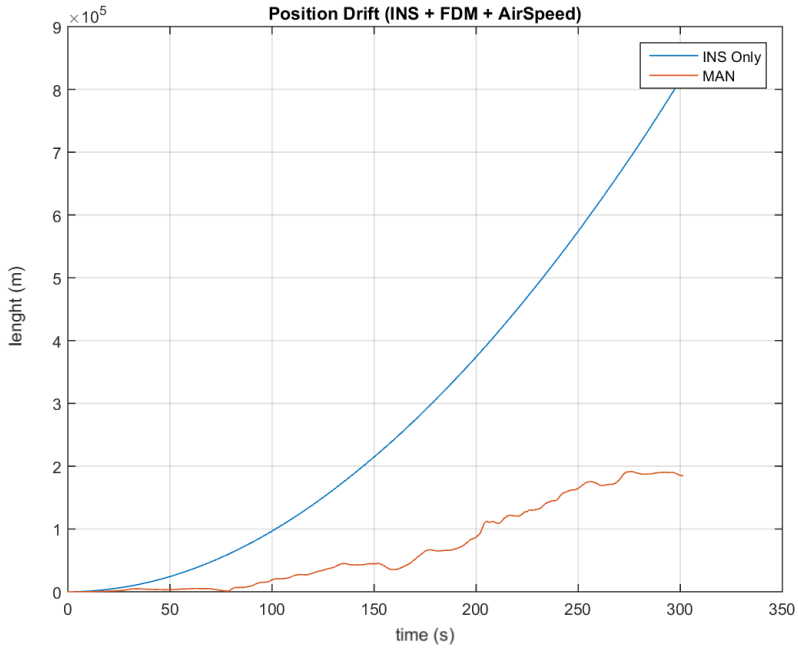

Figure 4.9: Position drifts related of INS alone and MAN (INS+VDM+Airspeed architecture)

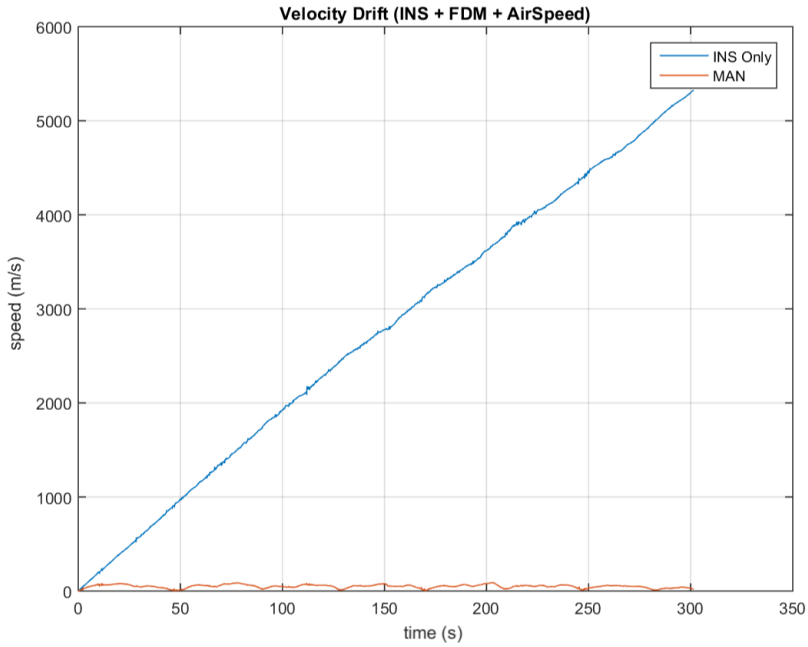

Figure 4.10: Velocity drifts related of INS alone and MAN (INS+VDM+Airspeed architecture)

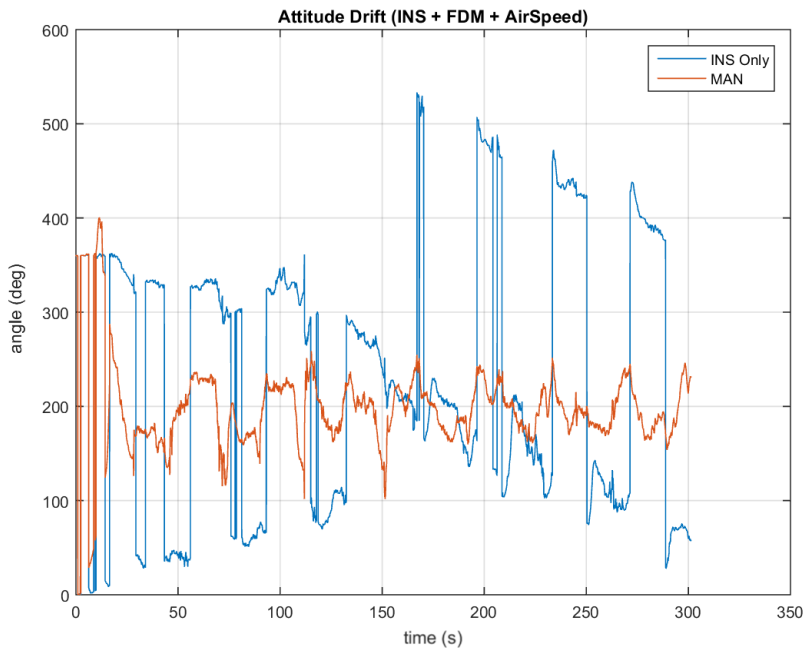

Figure 4.11: Attitude drifts related of INS alone and MAN (INS+VDM+Airspeed architecture)

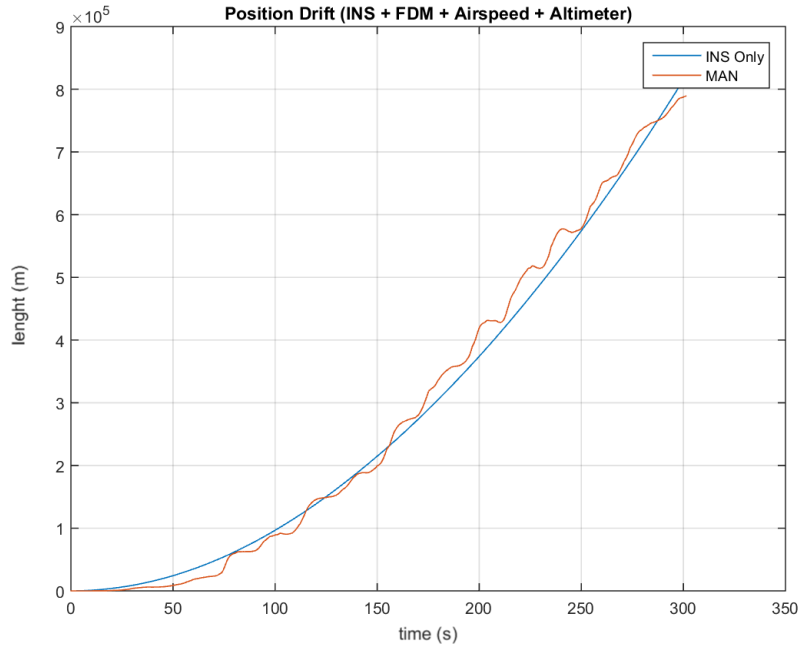

Figure 4.12: Position drifts related of INS alone and MAN (INS+VDM+Airspeed+Altimeter architecture architecture)

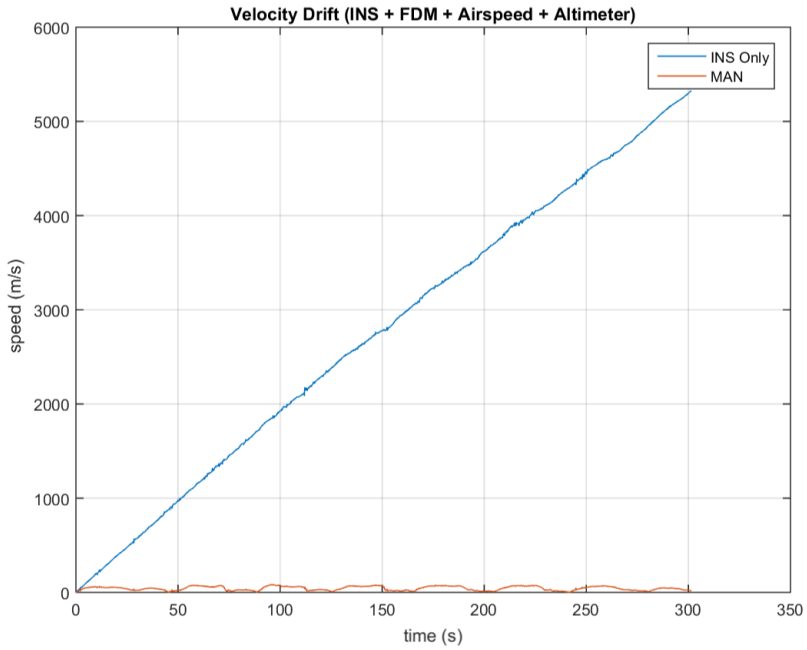

Figure 4.13: Velocity drifts related of INS alone and MAN (INS+VDM+Airspeed+Altimeter architecture architecture)

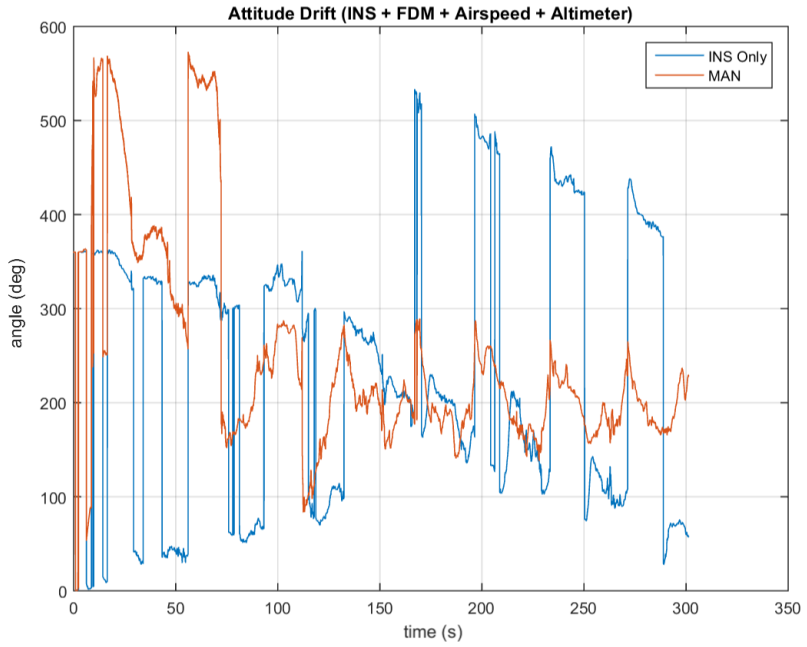

Figure 4.14: Attitude drifts related of INS alone and MAN (INS+VDM+Airspeed+Altimeter architecture architecture)

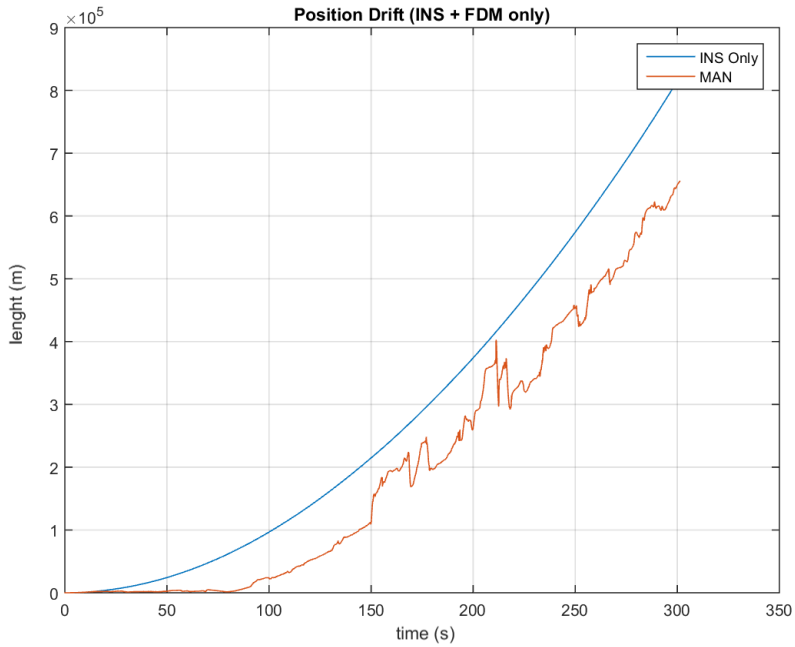

Figure 4.15: Position drifts related of INS alone and MAN (INS+VDM architecture), different Q and R

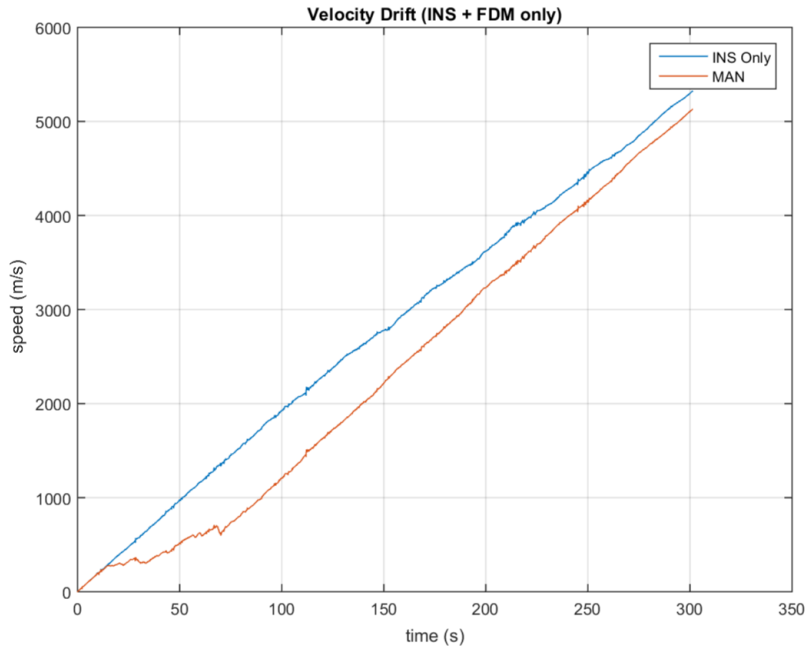

Figure 4.16: Velocity drifts related of INS alone and MAN (INS+VDM architecture), different Q and R

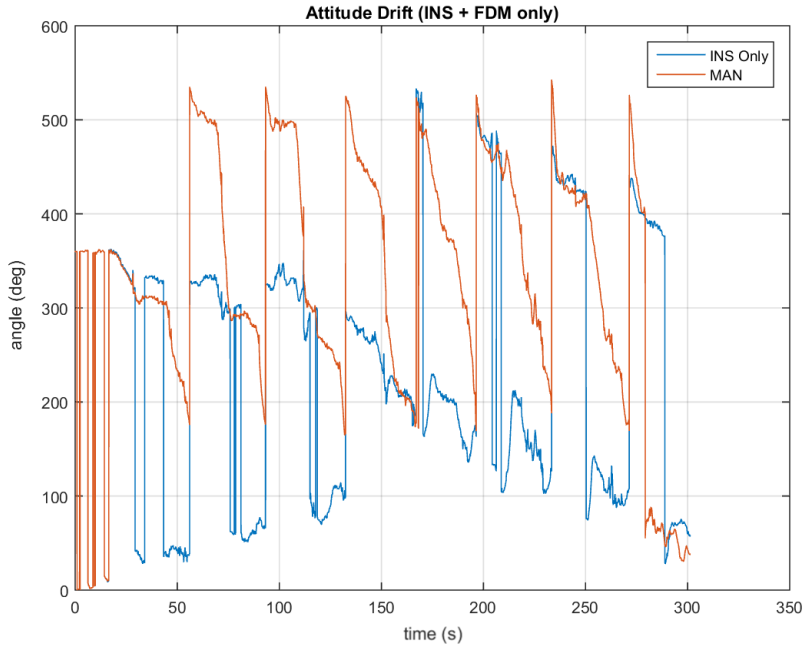

Figure 4.17: Attitude drifts related of INS alone and MAN (INS+VDM architecture), different Q and R

Table 4.9: Process noise covariance matrix Q and measurement noise covariance matrix R values for Flight Testing data INS+VDM only case

Process noise covariance matrix Q	Position	$5.6 \cdot 10^{-8}$ rad
	Velocity	$8 \cdot 10^{-4}$ m/s
	Attitude	$2.98560 \cdot 10^{-18}$ rad
	Angular Rates	2.07330 rad/s
Measurement noise covariance matrix R	Velocity	1 m/s
	Attitude	1 rad
	Angular Rates	1 rad/s
	Airspeed	4 m/s
	Altimeter	4 m

Chapter 5

Conclusions

This sensitivity study confirm that considering a VDM model coupled with an UKF and combined with an INS, we obtain a higher performance navigation system considering booth simulated and real flight data. VDM-only position, velocity and attitude solutions are improved, this approach lowers INS positing solution errors by up to one third to half over the 5 minute simulated flights. In every experimental setup, the introduction of an airspeed sensor gives benefits in terms of velocity estimation as the introduction of an altimeter does with position estimation (vertical-axis NED component in particular of course). The scaled aerodynamic model influences the position more than the velocity solution. As expected, the performance increases in terms of position and Attitude estimation using a better IMU, however when used MAN, the impact is apparent for positioning.

The empirical tuning of the Q and R matrices influence the overall result considerably. In this case deeper investigation to try to optimize the Q and R in order minimize the estimations can be performed.

Future developments will involve the introduction in the model of winds, gusts and turbulence. A study about how different maneuver sequences and flight conditions affect the results of the proposed approach can be performed.

Complete CFD analysis and wind tunnel tests can be considered in the future as additional aerodynamic models to be compared with the reference model used in this work and subsequently they could be used to investigate their influence on the MAN approach proposed.

Appendices

Appendix A

The Testbed parts

In the following section, details of the Phastball Zero components illustrated in Figure (2.5 on page 6) are reported.

Table A.1: HET650-58-1970 (motor) characteristics [24]

Diameter	36 mm
Length	57.50 mm^2
Shaft Diameter	5 mm^2
Weight	250 g
Internal resistance	12
No load current (lo)	2.3
Max efficiency	88%
Poles	4
No load KV	1970
Suggested lipo cells	6S
Maximum amps:	100 A (6S)
Power Nominal:	2200 W

Table A.2: ADIS16485 (IMU) characteristics [25]

Gyro Bias Repeatability	$\pm 0.200°/s$
Gyro Bias In-run Stability	6.500 °/h (1σ)
Angular Random Walk (ARW)	$0.300\,°/\sqrt{\text{h}}$ (1σ)
Accel Bias Repeatability	± 3 mg
Accel Bias In-run Stability	32 µg (1σ)
Velocity Random Walk (VRW)	$0.023 \quad \text{m/s}/\sqrt{\text{h}}$

Table A.3: STI22FS-5 (potentiometer) characteristics [26]

Electrical Angle	100°
Mechanical Angle	360° (continuous)
Supply Voltage	5 V ± 10%
Output	0.5 ∼ 4.50 V
Linearity	±0.5%
Turns Life	100000000
Body dia.	22 mm
Shaft Diameter	3 mm
Shaft Length	11.50 mm
IP Rating	IP40

Table A.4: MPXV7002 (pitot) characteristics [27]

Range	-2 to 2 kPa
Output	0.5 to 4.500 V
Weight	4 g

Table A.5: OEM 615 (GPS Novatel) characteristics [28]

Horizontal Position Accuracy	
Single Point L1	1.50 m L1/L2
Single Point L1/L2	57.50 mm^2
SBAS	5 mm^2
DGPS	250 g
Measurement Precision	
L1 C/A code	4 cm (GPS) 8 cm (GLO)
L1 carrier phase	0.5 mm (GPS) 1 mm (GLO)
L2 P(Y) code	8 cm (GPS) 8 cm (GLO)
L2 carrier phase	1 mm (GPS) 1 mm (GLO)
L2C code	8 cm (GPS) 8 cm (GLO)
L2C carrier phase	1 mm (GPS) 1 mm (GLO)
Maximum Data Rate	
Measurements	50 Hz
Position	50 Hz
Signal Reacquisition	
L1	< 0.5 s (typical)
L2	< 1.0 s (typical)
Time to First Fix	< 50 s (Cold start) < 35 s (Hot start)
Time Accuracy	20 ns RMS
Velocity Accuracy	0.03 m/s RMS
Velocity Limit	515 m/s

Table A.6: EVK-M8T (u-blox) characteristics [29]

Serial Interfaces	1 USB V2.0
	1 RS232, max. baud rate 921,6 kBd
	DB9 +/- 12 V level
	14 pin -3.3 V logic
	1 DDC (I2C compatible) max. 400 kHz
	1 SPI – clock signal max. 5,5 MHz
	SPI DATA max. 1 Mbit/s
Timing Interfaces	2 Time-pulse outputs
	1 Time-mark input
Dimensions	105 x 64 x 26 mm
Power Supply	5V via USB or external powered via extra power supply
	pin 14 (V5_IN) 13 (GND)
Normal Operating temperature	40°C to +65°C

Table A.7: MOD54415-100IR (NetBurner) characteristics [30]

Processor and Memory	32-bit Freescale ColdFire 54415 running at 250MHz with 64MB DDR2 RAM and 32MB Flash
Network Interface	10/100 BaseT with RJ-45 connector
Data I/O Interface (J1)	Up to 8 UARTs
	Up to 4 I2C
	Up to 2 CAN 2.0b controllers
	Up to 3 SPI
	Up to 42 digital I/O + 2 digital inputs
	Up to eight 12-bit analog-to-digital converters (ADC)
	Up to two 12-bit digital-to-analog converters (DAC)
	Up to 5 pulse width modulators (PWM)
	Up to 4 external timer in or outputs
	MicroSD flash card ready
	1-Wire® interface
Flash Card Support	FAT32 support for SD Cards up to 32GB
Serial Configurations (UART)	8 TTL ports
	Add external level shifter for RS-232
	Add external level shifter for RS-422/485
LEDs	Link and Speed
Physical Characteristics	2.95 x 2.00 in
Weight	1 oz
Mounting Holes	3 x 0.125 in dia.
Power	3.3VDC @ 410 mA with Ethernet
	3.3VDC @ 360 mA without Ethernet

Table A.8: Spektrum AR12120 (Receiver) characteristics [31]

# of Channels	12
Modulation	DSM2/DSMX
Band	2.4GHz
Length	2.05 in (52.0mm)
Width	1.83 in (46.5mm)
Height	0.60 in (15.3mm)
Weight	2.54 oz (72 g)
Voltage Range	6-10 V
Antenna Length	31 mm

Table A.9: ISS-D60 (Sun Sensor) characteristics [32]

Sensor type	2 axes Orthogonal
Field of view (FOV)	120° Aperture of the cone of view
Accuracy	$< 0.40°$ 3σ
Precision	$< 0.06°$ Sensitivity
Average consumption	33 mA
Diameter	80 mm
Height	27 mm
Weight	100 g
Level of protection	IP65 CEI 60529 Standard
Pressure	Tested at 0,05 mbar and 25°C

Table A.10: Spektrum DX9 (Transmitter) characteristics [33]

# of Channels	9
Modulation	DSM2/DSMX
Band	2.4GHz
Receiver	AR9020 9-Channel DSMX X-Plus Receiver
Programming Features	Airplane/Helicopter/Sailplane
Model Memory	250
Modes	User Selectable Mode 1-4
Transmitter (Tx) Battery Type	Lithium Ion Battery
Experience Level	Advanced

Appendix B

Aerodynamics

B.1 Airfoils

The wing airfoil, shown in the figure (B.1), is a NACA 2410.

Figure B.1: Wing airfoil NACA 2410

The horizontal tail airfoil, shown in the figure (B.2), is a NACA 0009.

Figure B.2: Horizontal Tail airfoil NACA 0009

Bibliography

[1] M. Koifman and I. Y. Bar-Itzhack, "Inertial navigation system aided by aircraft dynamics," *IEEE Transactions on Control Systems Technology*, vol. 7, no. 4, 1999.

[2] P. Crocoll, L. Görcke, G. F. T. Lorenz, and F. Holzapfel, "Unified model technique for inertial navigation aided by vehicle dynamics model," *Journal of Institute of Navigation*, vol. 60, no. 3, pp. 179–193, 2013.

[3] P. Crocoll, J. Seibold, G. Scholz, and G. F. Trommer, "Model-aided navigation for a quadrotor helicopter: A novel navigation system and first experimental results," *Journal of Institute of Navigation*, vol. 61, no. 4, pp. 253–271, 2014.

[4] M. Bryson and S. Sukkarieh, "Vehicle model aided inertial navigation for a uav using low-cost sensors," in *Proceedings of the Australasian Conference on Robotics and Automation*, 2004.

[5] F. Cappello, S. Ramasamy, and R. Sabatini, "A low-cost and high performance navigation system for small rpas applications," *Aerospace Science and Technology*, vol. 58, pp. 529–545, 2016.

[6] M. Khagani and J. Skaloud, "Autonomous vehicle dynamic model-based navigation for small uavs," *Journal of Institute of Navigation*, vol. 63, no. 3, pp. 345–358, 2016.

[7] S. D'Urso and J. Gross, "Sensitivity of unmanned aerial vehicle model-aided navigation," *AIAA Modeling and Simulation Technologies Conference*, 2017.

[8] Y. Gu, J. Gross, F. Barchesky, H. Chao, and N. M., "Avionics design for a sub-scale fault-tolerant flight control test-bed," *Recent Advances in Aircraft Technology.*

[9] J. Gross, Y. Gu, R. Watson, and S. D'Urso, "Flight-test evaluation of kinematic precise point positioning of small uavs," *International Journal of Aerospace Engineering*, vol. 7.

[10] R. F. Stengel, *Flight Dynamics*. Princeton University Press, 2004.

[11] C. Sequeira, D. J. Willis, and J. Peraire, "Comparing aerodynamic models for numerical simulation of dynamics and control of aircraft," in *44th AIAA Aerospace Sciences Meeting and Exhibit*, (Reno, NV), AIAA, 2006.

[12] M. R. Napolitano, *Aircraft Dynamics: from Modeling to Simulation*. Wiley, 2011.

[13] *Boundary layer thickness*. https://en.wikipedia.org/wiki/Boundary_layer_thickness.

[14] *Athena Vortex Lattice*. http://web.mit.edu/drela/Public/web/avl/.

[15] J. E. Williams and S. R. Vukelich, *The USAF Stability and Control Digital Datcom: Users manual*. No. v. 1, Air force flight dynamics laboratory, Air force Wright aeronautical laboratories, Air force systems command, 1976.

[16] P. D. Groves, *Principles of GNSS, inertial, and multisensor integrated navigation systems*. Artech House, 2013.

[17] E. A. Wan and R. van der Merwe, "The unscented kalman filter," *Chap. 7 in "Kalman Filtering and Neural Networks""*, pp. 221–282, 2002.

[18] J. Gross, Y. Gu, M. Rhudy, S. Gururajan, and N. M., "Flight test evaluation of sensor fusion algorithms for attitude estimation," *IEEE Transactions on Aerospace Electronic Systems*, vol. 48, 2012.

[19] M. Rhudy, Y. Gu, J. Gross, S. Gururajan, and N. M., "Sensitivity analysis of extended and unscented kalman filters for attitude estimation," *Journal of Aerospace Information Systems*, vol. 10, no. 3, pp. 131–143, 2013.

[20] D. Simon, *Optimal state estimation: Kalman, H infinity, and nonlinear approaches*. John Wiley & Sons, 2006.

[21] "Flightgear flight simulator," version 3.4.0 (2015). http://www.flightgear.org/.

[22] *Louis Bennett Field*. https://en.wikipedia.org/wiki/Louis_Bennett_Field.

[23] "Hg1930 inertial measurement unit," Honeywell International, Inc. https://aerospace.honeywell.com/~/media/aerospace/files/brochures/n61-1025-000-001-hg1930-bro.pdf.

[24] *HET-650-58-1970 Motor Data Sheet*. P3 America Inc. http://www.effluxrc.com/HET-650-58-1970-Motor-HET650-58-1970.htm.

[25] *Analog Device ADIS16485 Tactical Grade, Six Degrees of Freedom Inertial Sensor - Data Sheet*. http://www.analog.com/media/en/technical-documentation/data-sheets/ADIS16485.pdf.

[26] *STI22FS-5*. http://p3america.com/products/index.php?main_page=product_info&products_id=720,.

[27] *Hobbyking Pitot*. https://hobbyking.com/en_us/hk-pilot-analog-air-speed-sensor/and-pitot-tube-set.html.

[28] *Receivers OEM615*. Novatel. https://www.novatel.com/assets/Documents/Papers/OEM615.pdf.

[29] *EVK-M8T Evaluation Kit User Guide*. u-blox. https://www.u-blox.com/sites/default/files/products/documents/EVK-M8T_UserGuide_%28UBX-14041540%29.pdf.

[30] *MOD5441X Single & Dual Port Ethernet Core Module Data Sheet*. https://www.netburner.com/index.php/support/documents/mod54415/255-1-7/file.

[31] *AR12120 Receiver*. Spektrum. https://www.spektrumrc.com/Products/Default.aspx?ProdID=SPMAR12120.

[32] *ISS-DX Technical Specifications*. http://www.solar-mems.com/wp-content/uploads/2017/02/ISSDX_Technical_Specifications.pdf.

[33] *DX9 Transmitter*. Spektrum. http://www.spektrumrc.com/Products/Default.aspx?ProdId=SPM9900.